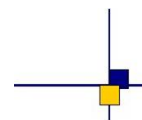


# Filtering ionospheric correction from altimetry dual-frequencies solution

From SLOOP project to integration in L2 products



---

Reference : SALP-NT-P-EA-23887-CLS

Date : March 22, 2021

---

Chronology Issues:		
Issue:	Date:	Reason for change:
	March 22, 2021	Creation

People involved in this issue :				
	AUTHORS	COMPANY	DATE	INITIALS
Written by:	F. Nencioli	CLS		
Checked by:	H. Roinard	CLS		
	M. Raynal	CLS		
Approved by:		CLS CLS		
Application authorised by:				

Index Sheet :	
Context:	
Keywords:	
Hyperlink:	

Distribution:		
Company	Means of distribution	Names
CLS/DOS	electronic copy	V.ROSMORDUC
CNES	electronic copy	thierry.guinle@cnes.fr francois.bignalet-cazalet@cnes.fr nicolas.picot@cnes.fr gerald.dibarboure@cnes.fr aqgp_rs@cnes.fr dominique.chermain@cnes.fr delphine.vergnoux@cnes.fr

**List of tables and figures**

**List of Tables**

1 Values of each variable used at different steps of the iterative filtering scheme for the production of Jason-3 GDR-F and Sentinel-3 products. . . . . 19

**List of Figures**

1 Dual-frequency ionospheric correction measured along Jason-1 track 004 during cycle 280. (Left) Track location. (Right) Along-track ionospheric correction values as a function of latitude (only values for valid altimetry observations are shown). This track will be used as an example throughout the report to highlight some of the features of the iterative filtering method. . . . . 2

2 Timeseries of number of observed sunspot for the last two cycles (23 and 24) of solar activity. Image from <https://solarscience.msfc.nasa.gov/>. . . . . 4

3 Timeseries of mean (left) and standard deviation (right) per cycle of the dual-frequency ionospheric correction for the TOPEX and the three Jason missions. . . . . 5

4 Timeseries of mean (left) and standard deviation (right) per cycle and per different local times of the dual-frequency ionospheric correction for the Jason-1 mission. . . . . 6

5 Maps of mean (left) and variance (right) per 2° by 2° areas of Jason-1 dual-frequency ionospheric correction for 2002. . . . . 6

6 Maps of mean (left) and variance (right) per 2° by 2° areas of Jason-1 dual-frequency ionospheric correction for 2009. . . . . 7

7 (Top) Map of variance difference between the SLA computed without a ionospheric correction and that computed using the raw ionospheric correction using Jason-1 2002 observations. (Bottom) Same as top panel, but with the variance difference normalized by the variance of the SLA computed without a ionospheric correction. In both maps, satellite observations are averaged over 2° by 2° areas. . . . . 8

8 (Top) Map of variance difference between the SLA computed without a ionospheric correction and that computed using the raw ionospheric correction using Jason-1 2009 observations. (Bottom) Same as top panel, but with the variance difference normalized by the variance of the SLA computed without a ionospheric correction. In both maps, satellite observations are averaged over 2° by 2° areas. . . . . 9

9 Timeseries of mean (left) and standard deviation (right) per cycle of the low-frequency (red) and the high-frequency (blue) components of the Jason-1 dual-frequency ionospheric correction. . . . . 11

10 Timeseries of mean (left) and standard deviation (right) per cycle of the high-frequency components of the Jason-1 dual-frequency ionospheric correction for different local hours (blue and red curves). For comparison, the global curves (i.e. obtained using observations from all times of the day) are show in green. These correspond to the blue curves in Fig 9. . . . . 11

11 Maps of SWH (top) and high frequency component of the ionospheric correction (middle) from Jason1 cycle 270 (from 30 April to 10 May 2009). Observations are averaged over 2° by 2° areas. The variance of the ionospheric high frequency component is shown in the bottom panel. . . . . 13

12 Flowchart of the dual-frequency ionospheric correction filtering scheme . . . . . 15

13	Evolution of the dual-frequency ionospheric correction at different steps of the iterative filtering scheme for Jason-1 track 004 from cycle 280. (Top) All valid measurements selected after step 1. (Middle) Valid measurements retained after the robust filter is applied (red) and resulting median filtered correction (blue) at the end of step 5 for the first iteration. (Bottom) Final filtered and interpolated correction (blue) at the end of step 11 and all valid raw observations used to compute it (red). Note that the y-axis limits change between figures as outliers are progressively removed through the iterative filtering. . . . .	18
14	Maps of of variance difference (top) and percentage of variance difference (bottom) between the SLA computed without correction and that computed using the raw correction using Jason-3 observations from cycle 17 to cycle 58. In both maps, satellite observations are averaged over 2° by 2° areas. . . . .	21
15	Same as figure 14, but using the iterative filtered correction instead. . . . .	22
16	(Top) Maps of the difference between $\Delta VAR_{SLA}$ computed using the iterative filtered ionospheric correction (Figure 15, top) and that computed using the raw correction (Figure 14, top). (Bottom) Same as top panel, but for $\%VAR_{SLA}$ . In both maps, satellite observations are averaged over 2° by 2° areas. . . . .	23
17	Time series of the average SLA variance per cycle for Jason-3 observations from cycles 17 (2016/08) to 58 (2017/09). Blue curve is for SLA without any ionospheric correction; red curve is for SLA with the raw ionospheric correction; cyan curve is for SLA with the iterative filtered ionospheric correction. . . . .	25
18	Same as Figure 17, but for the full Jason-1 time series (cycles 1 to 375). Blue curve is for SLA without any ionospheric correction; red curve is for SLA with the raw ionospheric correction; cyan curve is for SLA with the iterative filtered ionospheric correction. . . . .	25
19	Distribution of points with edited ionospheric correction for Jason-3 GDR-F observations from cycle 20. Blue circle are points edited only using the iterative filtered correction; red circles are points edited only using the raw filtered correction; green circles are edited points common to both corrections. . . . .	27
20	Same as figure 14, but using Sentinel-3A SAR 1Hz observations. The observations are from cycles 7 to 21 covering the same period (2016/07 to 2017/09) as the Jason-3 data used in Section 4. . . . .	31
21	Same as figure 20, but using the iterative filtered correction instead. . . . .	32
22	Same as figure 16, but using Sentinel-3A SAR 1Hz observations as in figure 20. . . . .	33
23	Same as figure 17, but using Sentinel-3A SAR 1Hz observations as in figure 20. Blue curve is for SLA without any ionospheric correction; red curve is for SLA with the raw ionospheric correction; green curve is for SLA with the iterative filtered ionospheric correction. . . . .	34

**List of items to be defined or to be confirmed**

## Applicable documents / reference documents

[DA1](#) CLS-DOS-NT-10-0098 SALP-NT-P-EA-21834-CLS “SLOOP Tache 2.4 : Amélioration du filtrage de la correction ionosphérique bifréquence” M.ABLAIN, J.F. LECEAIS

## List of Acronyms

**ADT** Absolute Dynamic Topography  
**CLS** Collecte Localisation Satellites  
**CNES** Centre National d’Etudes Spatiales  
**DV** Default Value  
**EIA** Equatorial Ionosphere Anomaly  
**RMS** Root Mean Square  
**SSH** Sea Surface Height  
**SNR** Signal to Noise Ratio  
**SLA** Sea Level Anomaly  
**SSB** Sea State Bias  
**SWH** Significant Wave Height  
**TEC** Total Electron Content

## Contents

<b>1. General Presentation</b>	<b>1</b>
1.1. Context and goals of the study . . . . .	1
1.2. Overview of altimeter technology . . . . .	1
1.3. Dual-frequency ionospheric correction . . . . .	1
<b>2. Spatio-Temporal Characteristics of the Ionospheric Correction</b>	<b>4</b>
2.1. Temporal variability . . . . .	4
2.1.1. Solar activity dependency . . . . .	4
2.1.2. Local hour dependency . . . . .	5
2.2. Spatial distribution . . . . .	6
2.3. Explained SLA variance . . . . .	7
2.4. High frequency content of the ionospheric correction . . . . .	10
<b>3. The Iterative Filter Method</b>	<b>14</b>
3.1. Algorithm description . . . . .	14
3.2. Jason-3 and Sentinel-3 specifications . . . . .	19
<b>4. Evaluation of the iterative filtering on Jason-3 GDR-F observations</b>	<b>20</b>
4.1. Explained SLA with respect to raw correction . . . . .	20
4.1.1. Spatial distribution . . . . .	20
4.1.2. Temporal variability . . . . .	24
4.2. Number of points edited by the algorithm . . . . .	26
<b>5. Conclusions</b>	<b>29</b>
<b>Appendix A. Evaluation of the iterative filtering on Sentinel-3A observations</b>	<b>30</b>

## 1. General Presentation

### 1.1. Context and goals of the study

This report aims to describe the iterative filtering method applied to the ionospheric correction in the production of Sentinel-3 and Jason-3 GDR-F altimetry products. The method was developed at Collecte Localisation Satellites (CLS) in 2010 within the context of the SALP study commissioned by Centre National d'Etudes Spatiales (CNES). A first description of the method was provided in the [SALP-NT-P-EA-21834-CLS](#) report (French only). Here we present an updated overview of the main results from that report with the goal of providing a useful and much needed reference for the broader international altimetry community on the ionospheric correction iterative filtering.

In this report, readers will be first presented with the general characteristics of the ionospheric correction signal, its spatio-temporal variability and its impact on the on-board altimeter measurements. The iterative filtering approach will be then described, and the advantages of such approach will be assessed by comparing the resulting sea level anomaly fields with those obtained using the unfiltered ionospheric correction. Justifications for the various choices at the base of the filter design will be provided whenever possible. Limitations of the current design and aspects still open for further improvements will be discussed in the **Conclusions** section.

### 1.2. Overview of altimeter technology

An on-board altimeter is a satellite instrument primarily used to measure the Sea Surface Height (SSH) either relative to an observed mean elevation (the so called Sea Level Anomaly (SLA)) or relative to the geoid (the so called Absolute Dynamic Topography (ADT)). The instrument works by first sending an electromagnetic pulse through the atmosphere and then measuring the received response after the pulse is reflected by the surface of the ocean and propagates back to the satellite. If the electromagnetic signal travelled at the speed of light in the void, the distance between the satellite and the ocean would simply be the speed of light multiplied by half the travel time. However, the electromagnetic signal is slowed down by various elements present in the atmosphere. Thus, this induced delay must be accounted for in the distance computation. The electron activity in the ionosphere – the part of Earth's upper atmosphere ionized by solar radiation – plays an important role in delaying an altimeter pulse propagation, accounting for errors of more than 10 cm in the evaluation of the distance between the satellite and the ocean surface [1].

### 1.3. Dual-frequency ionospheric correction

To measure the delay of pulse propagation induced by the ionosphere, satellite altimeters use observations from two signals emitted at the same time at two different frequencies. These correspond to the wavebands  $-Ku$  and  $-C$  in the case of the Jason and Sentinel-3 missions. The main waveband  $-Ku$  is set to 13.575 GHz (bandwidth 350 MHz) for both Sentinel-3 and Jason, and the secondary waveband  $-C$  is 5.41 GHz (bandwidth 320 MHz) for Sentinel-3 and 5.3GHz for Jason. Because of the frequency difference, the two signals are differently delayed as they cross the ionosphere. The ionospheric correction can thus be estimated as a function of the difference in delay between the two signals after the Sea State Bias (SSB) corrections are applied. Thus, such correction is called dual-frequency ionospheric correction:

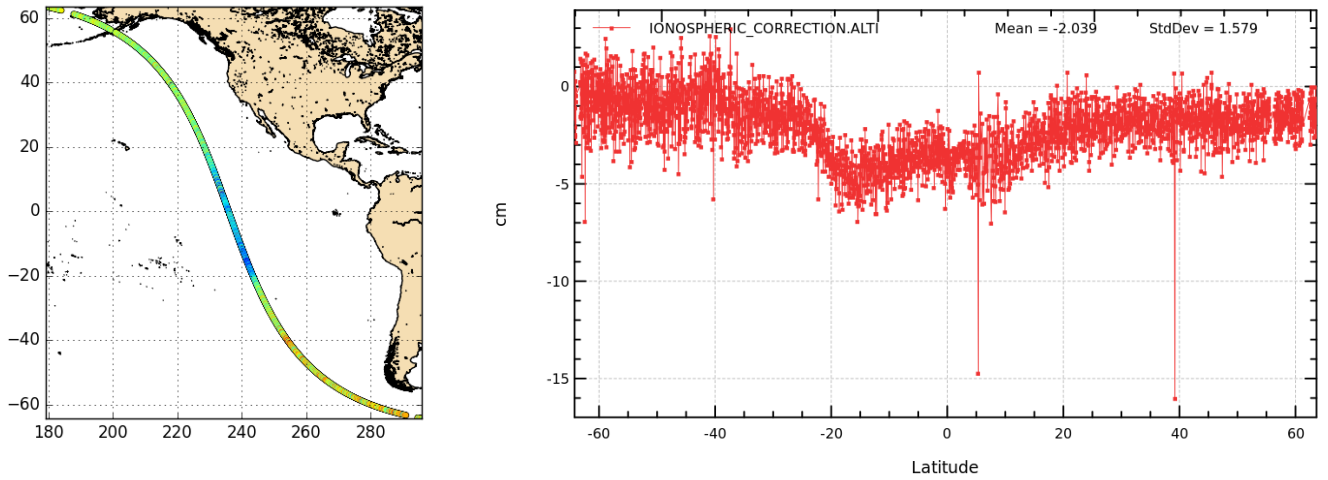


Figure 1 – Dual-frequency ionospheric correction measured along Jason-1 track 004 during cycle 280. (Left) Track location. (Right) Along-track ionospheric correction values as a function of latitude (only values for valid altimetry observations are shown). This track will be used as an example throughout the report to highlight some of the features of the iterative filtering method.

$$\text{Iono} = \delta f[(\text{Range}_{\text{Ku}} + \text{SSB}_{\text{Ku}}) - (\text{Range}_{\text{C}} + \text{SSB}_{\text{C}})] \quad (1)$$

$$\text{with } \delta f = \frac{f_c^2}{f_{\text{Ku}}^2 - f_c^2}$$

This leads to a  $\delta f$  value of 0.1798 in case of Jason and 0.1889 in case of Sentinel-3.

As an example, Figure 1 shows the dual-frequency ionospheric correction measured by Jason-1 along track 004 during cycle 280. The correction ranges from average values of roughly  $-1$  cm at high latitudes to minimum values of  $-5$  cm within the tropics. This spatial distribution is typical for this correction and results from a combination of its geographical and temporal variability that will be discussed in more detail in Chapter 2. The measurements are also characterized by a high level of noise (on the order of 1 cm) along the whole track, as well as by few outlier measurements. These are also typical features for the correction. The noise comes partly from measurement errors in the ranges of the two bands but also from the choice of SSB correction algorithm used in Equation 1. It is to reduce the impact of these errors and improve the quality of the final altimetry products that a filtering of the dual-frequency ionospheric correction is required. Since studies based on TOPEX observations [2, 3] showed that such errors essentially lay in the high frequency content of the ionospheric correction signal, the initial recommendation was to smooth the correction over 200 km along-track. Further refinements of the filtering method lead to the iterative filtering scheme described in this report.

**Summary:** The ionospheric correction is inherently noisy since it includes measurements errors from two different frequency bands ( $K_u$  and  $C$ ), as well as errors associated with the choice of the SSB correction algorithm applied. To mitigate the impact of these errors on the final altimetry products, the use of filtering is thus required and justified.

The report will be structured in 3 parts:

1. **Characterization** of the spatio-temporal distribution and variability of the ionospheric correction
2. **Description** of the iterative filter method
3. **Assessment** of the performance of the filtered correction with respect to the raw correction

Hereafter, unfiltered ionospheric measurements will be referred to as “raw ionospheric correction/content”.

## 2. Spatio-Temporal Characteristics of the Ionospheric Correction

The delay of pulse propagation induced by the ionosphere is proportional to its Total Electron Content (TEC). Since ionization in the upper part of the atmosphere is primarily due to ultraviolet radiation from the sun, TEC and hence the ionospheric correction are characterized by spatial patterns and temporal variability tightly linked to those of solar conditions. In this chapter we will provide a quickly overview of such patterns and variability using the raw observations of dual-frequency ionospheric correction. Their characteristics will be particularly relevant to better understand some of the choices at the base of the iterative filter design described in Chapter 3.

### 2.1. Temporal variability

The two main sources of temporal variability of the dual-frequency ionospheric correction are associated with the solar activity cycle (Section 2.1.1.) and the diurnal cycle (Section 2.1.2.). The seasonal cycle is also likely to have an influence on the correction values. However, it was not investigated during the design of the iterative filter, and as such will not be discussed in this report.

#### 2.1.1. Solar activity dependency

The solar activity (measured in terms of variations in the number of observed sunspots on the solar surface) and, hence, the emitted solar radiation are characterized by a cycle of  $\sim 11$  years (variable from 8 to 15 years). The latest two major peaks of activity were observed between 2000 and 2002 and between 2013 and 2015 (Fig 2). Minimal activity was recorded between 2007-2009.

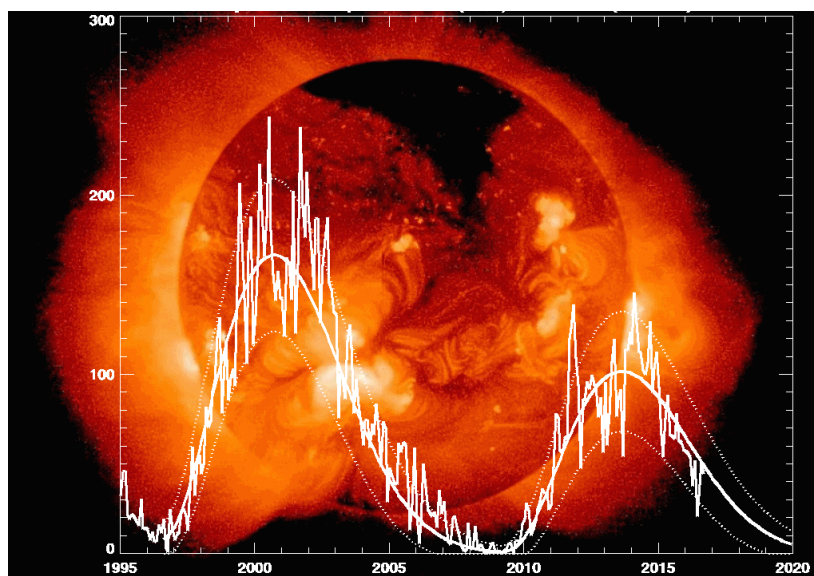


Figure 2 – Timeseries of number of observed sunspot for the last two cycles (23 and 24) of solar activity. Image from <https://solarscience.msfc.nasa.gov/>.

Figure 3 (left) shows the time series of average dual-frequency ionospheric correction per cycle for the TOPEX and three Jason missions. The bias between the TOPEX and the Jason-1 series is  $\sim 1.16$  cm and it is due to an update of the GDR between the two missions. As expected, the largest absolute values of average correction occur between 2000 and 2002 and between 2013 and 2015, the periods of highest solar activity.

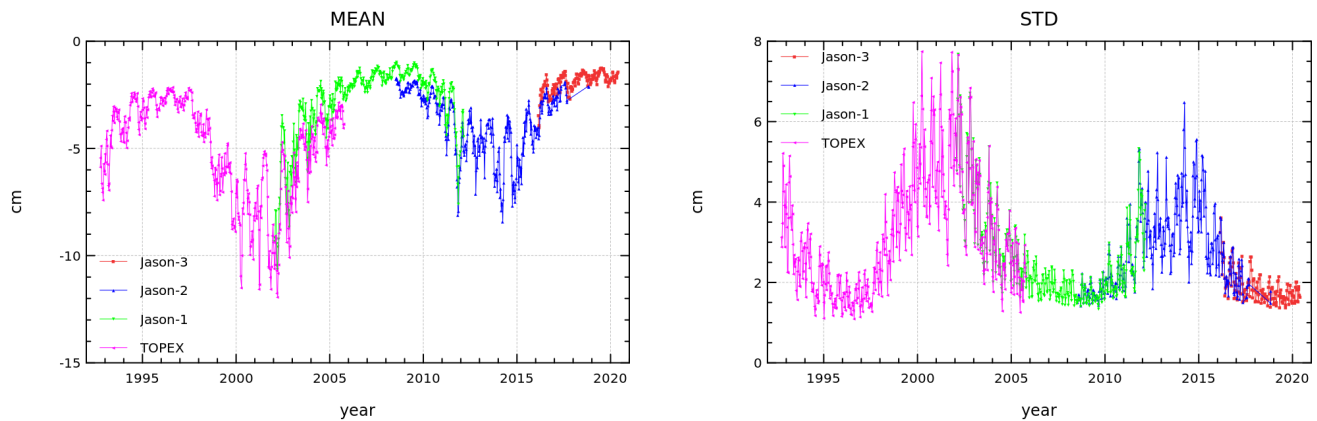


Figure 3 – Timeseries of mean (left) and standard deviation (right) per cycle of the dual-frequency ionospheric correction for the TOPEX and the three Jason missions.

Average values per cycle can exceed 10 cm in years of high solar activity and drop to less than 2 cm when solar activity is low. Inter-solar cycle variability is also observed with absolute values of the correction being much smaller between 2013 and 2015 than between 2000 and 2002. This is consistent with a lower level of solar activity observed during the 2013 to 2015 peak.

The timeseries of standard deviation (Figure 3, right) follows a similar pattern: variability is largest during years of high solar activity due to larger differences between day and night values (see Section 2.1.2.) as well as due to larger latitudinal differences observed in year of intense solar activity (see Section 2.2.).

During the rest of the chapter, we will focus on Jason-1 observations because they span over the largest solar activity differences (between 2002 and 2009).

### 2.1.2. Local hour dependency

As TEC depends on solar radiation, the ionospheric correction is also influenced by the diurnal cycle. The correction varies depending on the local time of acquisition: it increases during the day (peak at around 14:00 local time) and decreases at night (minimum at around 2:00 local time). Another factor influencing the values of the correction are the so called ionospheric scintillations – i.e. rapid modification of radio waves caused by small scale structures in the ionosphere. Scintillations determine sharp peaks in the correction thus increasing both its mean values and variability. They most frequently occur in the hours immediately after sunset and their impact is maximum within the tropical latitudinal band.

Figure 4 (left) shows the timeseries of average dual-frequency ionospheric correction per cycle and per different local times for the Jason-1 mission. The 02H\_06H average includes only observations collected between 2:00 and 6:00 local time, and thus corresponds to local night correction (with minimum impact due to scintillations). The 10H\_14H average includes only observations collected between 10:00 and 14:00 local time, and thus corresponds to local day correction. As expected, absolute values of ionospheric correction are much smaller during local nights than local days: night corrections during periods of high solar activity are of the same order as the day corrections during periods of low solar activity. As in Figure 3, the largest absolute values of local average correction occur in 2002 and 2012.

Standard deviation (Figure 4, right) also follows a similar pattern: variability is larger during local day hours and for years of high solar activity, most likely due to the larger latitudinal gradients occurring under those

conditions (see Figures 5 and 6).

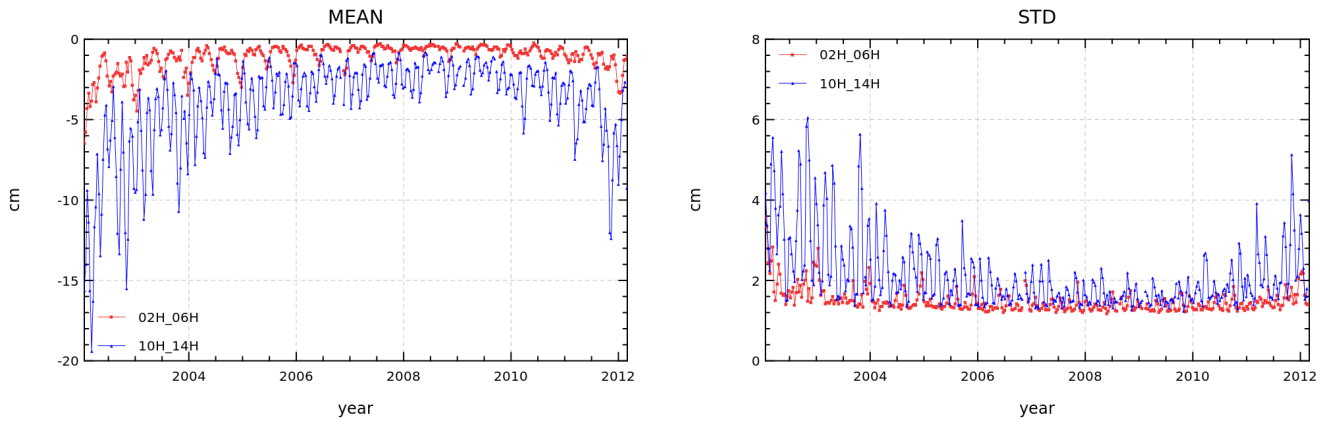


Figure 4 – Timeseries of mean (left) and standard deviation (right) per cycle and per different local times of the dual-frequency ionospheric correction for the Jason-1 mission.

## 2.2. Spatial distribution

The spatial distribution of TEC is primarily driven by the variations in solar radiation due to the changes in solar zenith angle with latitude, but geomagnetic activity and lower atmosphere meteorology also contribute [4]. Overall, TEC is minimum at high latitudes (low zenith angles) and increases towards the tropics (high zenith angles). Maximum values are found at roughly  $\pm 15^\circ$  of latitude, while are slightly lower at the equator values (the so called Equatorial Ionosphere Anomaly (EIA)).

The left panels in figures 5 and 6 show the spatial distribution of Jason-1 dual-frequency ionospheric correction respectively over year 2002 and 2009, averaged over areas of  $2^\circ$  by  $2^\circ$ . Both maps show smaller values at high latitude and larger values within the tropics, with maximum values within two bands north and south of the equator, typical for the EIA. Absolute values for 2002 are much larger than for 2009 (up to 10 cm) due to the higher solar activity (see Figure 3).

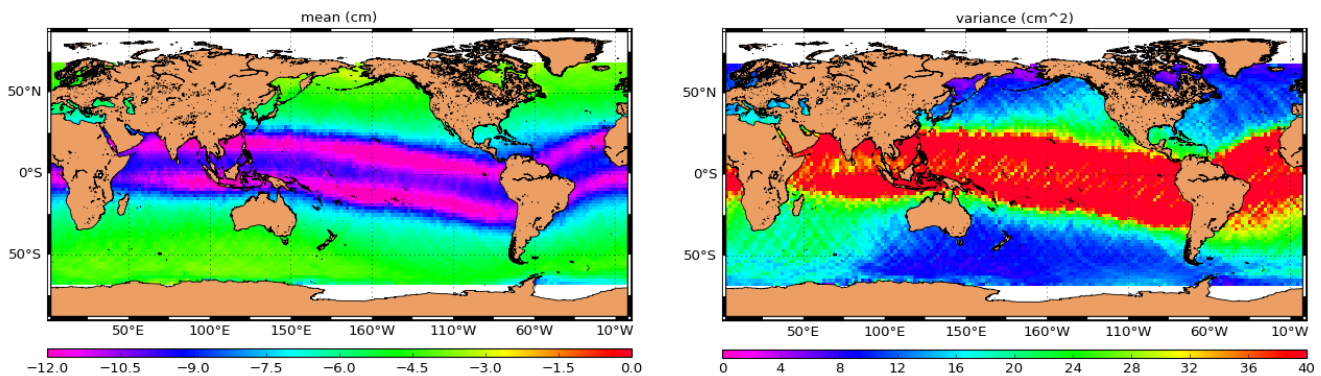


Figure 5 – Maps of mean (left) and variance (right) per  $2^\circ$  by  $2^\circ$  areas of Jason-1 dual-frequency ionospheric correction for 2002.

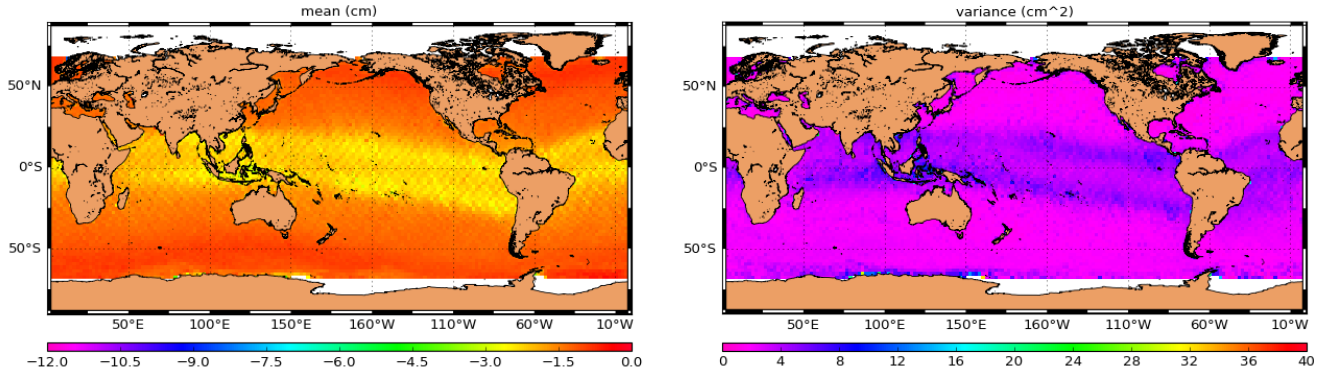


Figure 6 – Maps of mean (left) and variance (right) per 2° by 2° areas of Jason-1 dual-frequency ionospheric correction for 2009.

Similar maps for the variance (figures 5 right and 6 right) show analogous patterns (as already observed for the figures in Section 2.1.1. and 2.1.2.) both in terms of spatial distribution and decrease in magnitude from 2002 to 2009 due to the reduced solar activity.

### 2.3. Explained SLA variance

The dual-frequency ionospheric correction is one of the geophysical corrections applied to the range measured by the satellite altimeter to retrieve the SLA. Following [3], to investigate the impact of such correction on the final SLA, we analyse the explained variance. This is defined as the change in variance between the SLA computed without ionospheric correction and that computed with the raw ionospheric correction:

$$\Delta VAR_{SLA} = Var(SLA_{NoIono}) - Var(SLA_{RawIono}) \quad (2)$$

Thus,  $\Delta VAR_{SLA}$  indicates how much of the variance observed in the raw SLA observation is directly due to (or “explained by”) the presence of the ionosphere. When the explained variance is positive, the ionospheric correction reduces the SLA variance. Thus it improves the quality of the measurement since it reduces its uncertainty. On the other hand, when the explained variance is negative, the correction increases the SLA variance. In that case, it does not improve the quality of the measurement.

The top panel of figure 7 shows the explained variance averaged over areas of 2° by 2°, using Jason-1 observations from 2002. With the exception of the Indo-Pacific sector of the Antarctic Ocean and gulf of Carpentaria (north of Australia), values are always positive, with the maxima occurring within the tropics, where the ionospheric correction correction is also the highest.

To evaluate the importance of the variance reduction in different ocean regions, we also analysed the percentage of explained variance, defined as the explained variance normalized by the variance of the SLA computed without ionospheric correction:

$$\% VAR_{SLA} = \frac{Var(SLA_{NoIono}) - Var(SLA_{RawIono})}{Var(SLA_{NoIono})} \quad (3)$$

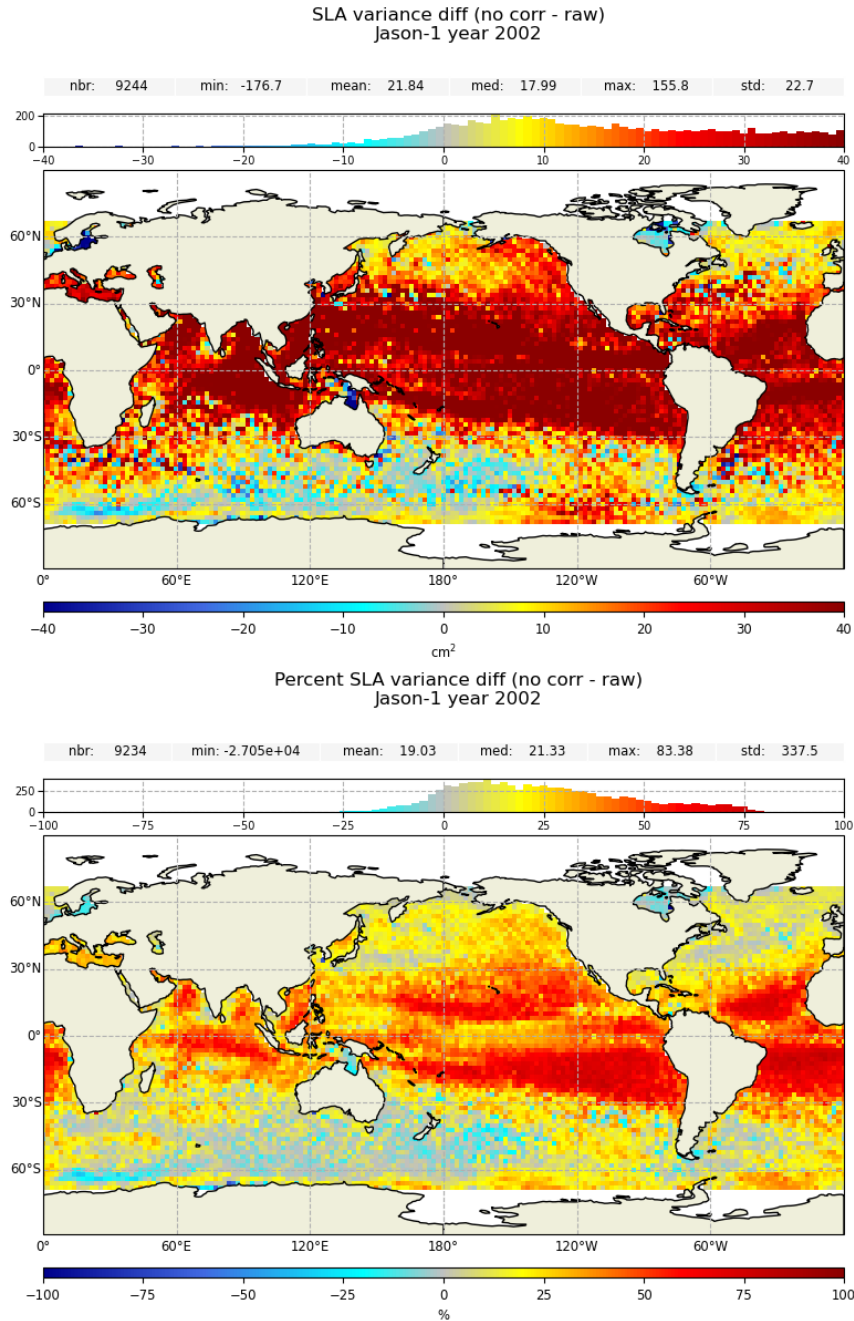


Figure 7 – (Top) Map of variance difference between the *SLA* computed without a ionospheric correction and that computed using the raw ionospheric correction using Jason-1 2002 observations. (Bottom) Same as top panel, but with the variance difference normalized by the variance of the *SLA* computed without a ionospheric correction. In both maps, satellite observations are averaged over 2° by 2° areas.

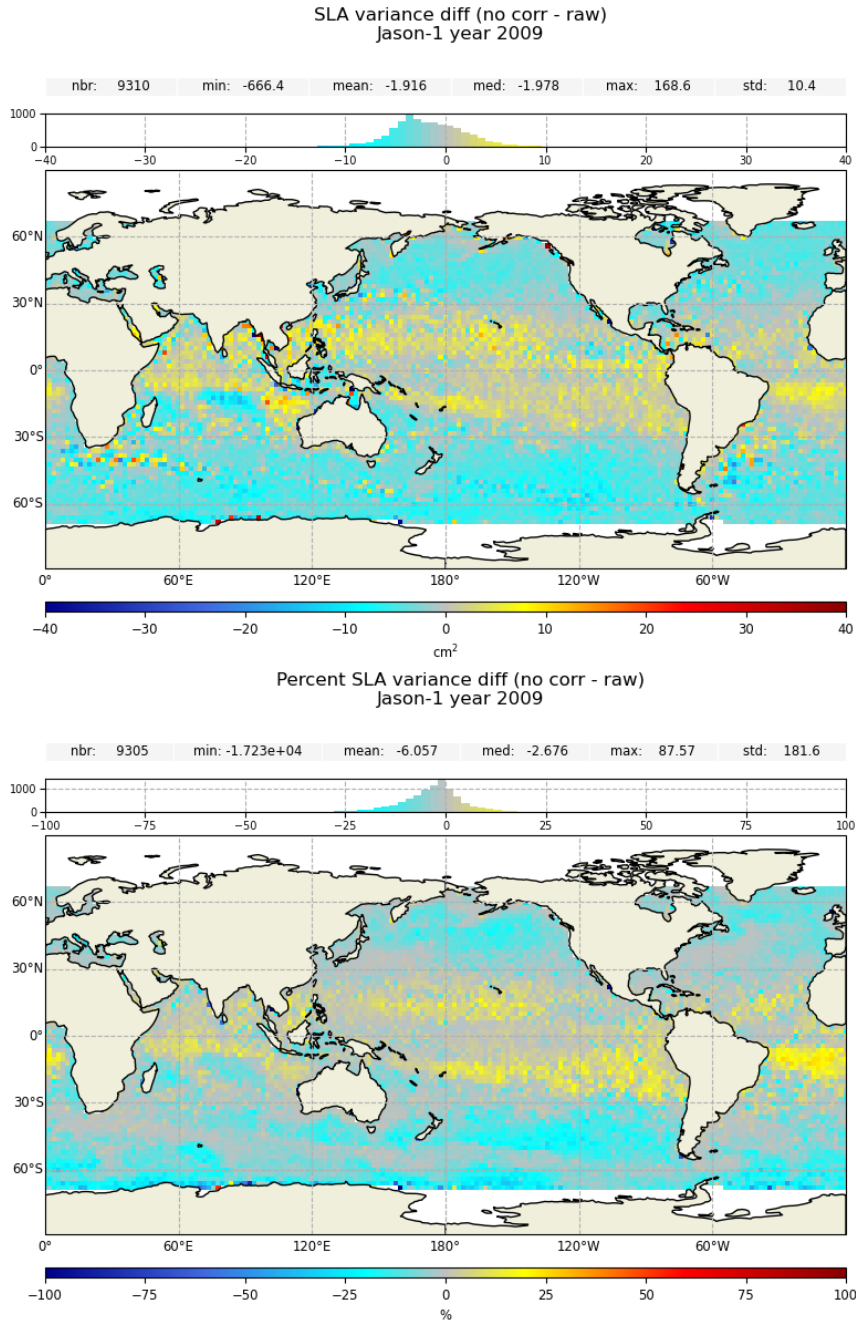


Figure 8 – (Top) Map of variance difference between the *SLA* computed without a ionospheric correction and that computed using the raw ionospheric correction using Jason-1 2009 observations. (Bottom) Same as top panel, but with the variance difference normalized by the variance of the *SLA* computed without a ionospheric correction. In both maps, satellite observations are averaged over 2° by 2° areas.

.....

The spatial distribution of  $\%VAR_{SLA}$  averaged over  $2^\circ$  by  $2^\circ$  areas using Jason-1 observations from 2002 is shown in figure 7, bottom. The map shows that despite the large differences observed in the top panel, the raw ionospheric correction contribute only to a modest reduction of the total variance in highly energetic ocean regions, such as western boundary currents, the Agulhas retroflexion and the Antarctic Circumpolar Current. That's because in those regions *SLA* variability is likely primarily controlled by mesoscale dynamics. On the other hand, the correction substantially reduces *SLA* variability in less energetic regions, and in particular within the tropics where the absolute values of correction are larger.

Both maps in figure 7 seem to suggest that simply applying the raw ionospheric correction is enough to improve the quality of *SLA* observations. However, maps of the same diagnostics computed from Jason-1 observations from 2009 show opposite results (figure 8): the raw ionospheric correction still improves *SLA* observations within the tropics, although to a much smaller extent than in 2002 (smaller positive values); however it degrades them almost everywhere else (negative values), with observed increases in variance up to 20% at high latitudes.

Overall, the raw ionospheric correction can improve *SLA* observations when its values are large (i.e. within the inter-tropical band, during years of high solar activity, at local day times) due to the higher Signal to Noise Ratio (*SNR*). However, it becomes ineffective (if not even detrimental) at high latitudes during years of low solar activity and/or at local night times when its values become of the same order as the background noise (low *SNR*; see figure 1).

Filtering the dual-frequency ionospheric correction is thus required to increase the *SNR* and, hence, improve the overall correction performance on *SLA* observations (and in particular in situations when correction values are low).

## 2.4. High frequency content of the ionospheric correction

---

To confirm that noise primarily lays in the high frequency content of the ionospheric correction, we applied a low-pass Lanczos filter on the correction and analysed the temporal variability of the filtered values (low frequency component) and their residuals (high frequency component). The filter cutoff length was set to 40 data points (approximately 230 km). This is in line with the  $\mathcal{O}(200)$  km filter length indicated in [3].

Figure 9 shows the average value per cycle (left panel) and the corresponding standard deviation (right panel) for the low and high frequency components of dual-frequency ionospheric correction obtained from Jason-1. The high frequency component shows mean values close to 0 ( $< 1\text{mm}$ ) for the whole period. Its standard deviation is also roughly constant throughout the time series, with small oscillations (of the order of 1 mm) around the average value of about 1.2 cm. Due to the almost null average values of the high frequency component, the low frequency component shows the same values and temporal variability as the total average shown in figure 3 (green curve), with the largest values observed during the years of higher solar activity. Similar temporal variability is also observed for the low frequency component standard deviation.

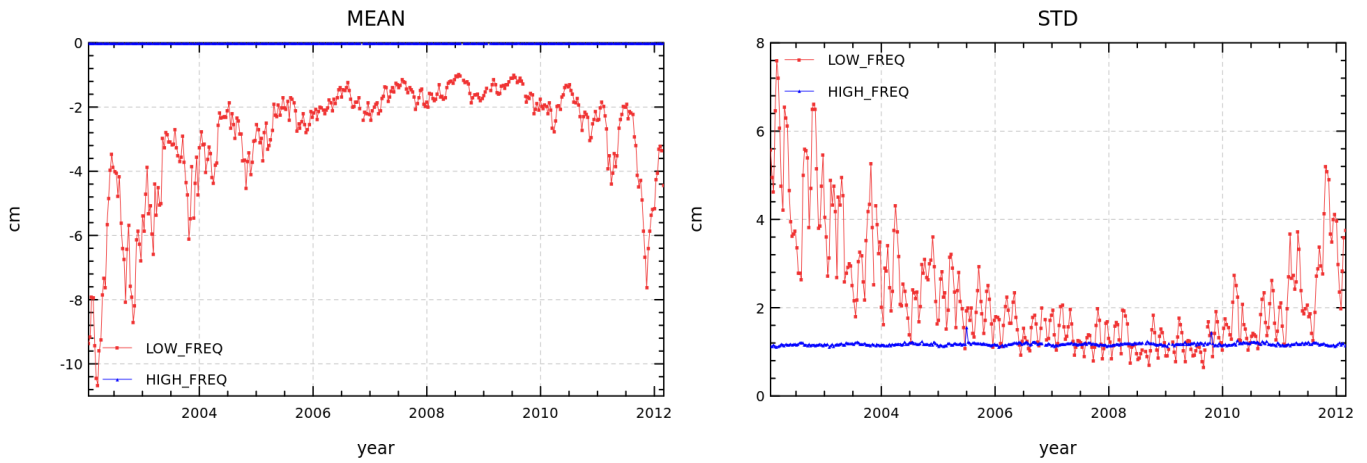


Figure 9 – Timeseries of mean (left) and standard deviation (right) per cycle of the low-frequency (red) and the high-frequency (blue) components of the Jason-1 dual-frequency ionospheric correction.

A more detailed analysis of the high frequency components is shown in Figure 10 where mean and standard deviations are computed for different local time intervals for day and night (analogous to the approach from Figure 4). Both time series indicate that the high frequency components are independent on the local time of the observations. However, mean and standard deviations show some interannual variability consistent between the different local hours as well as with the global curves (in green). While the variation observed in the average value is extremely small (of the order of 0.1 mm), the oscillations in the standard deviation are significantly larger (of the order of 1 mm), and thus they were further investigated.

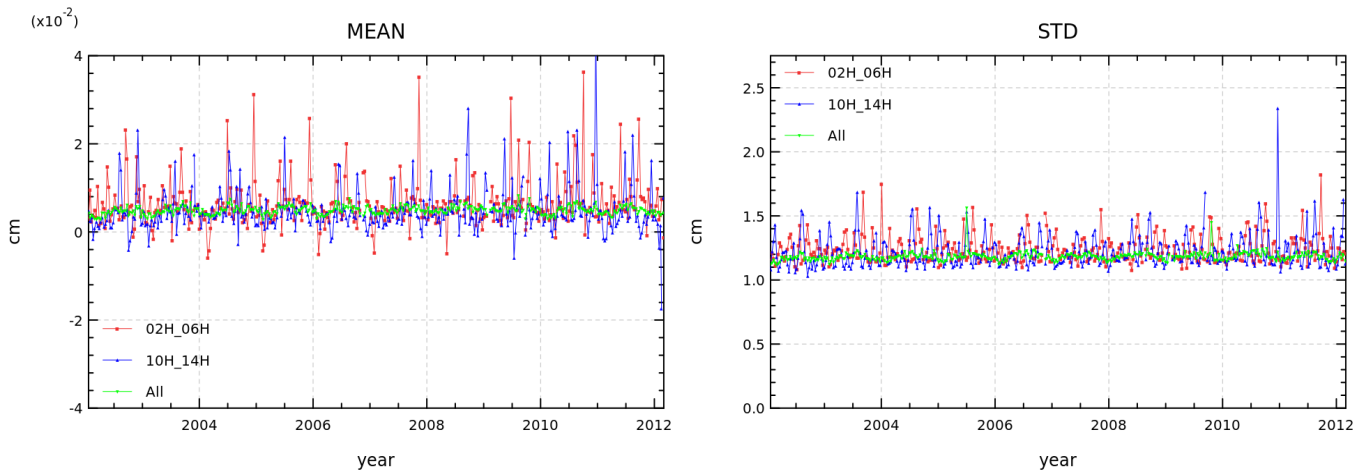


Figure 10 – Timeseries of mean (left) and standard deviation (right) per cycle of the high-frequency components of the Jason-1 dual-frequency ionospheric correction for different local hours (blue and red curves). For comparison, the global curves (i.e. obtained using observations from all times of the day) are show in green. These correspond to the blue curves in Fig 9.

Since the ionospheric correction is dependent on the accuracy of the **SSB** correction in both  $-Ku$  and  $-C$  bands (Eq. 1), potential correlations between the observed high frequency components and Significant Wave Height (**SWH**). Figure 11, shows maps of **SWH** (top) and high frequency ionospheric correction (middle) from Jason1 cycle 270 (30 April to 10 May 2009) averaged over areas of  $2^\circ$  by  $2^\circ$ , as well as the associated variance of high frequency ionospheric correction (bottom). Mean values of the high frequency component are uniformly close to 0 everywhere and do not show any spatial correlation with the **SWH** field. On the other hand, the variance of the high frequency component shows higher values where **SWH** is also large (e.g. Southern Ocean and Northeast Atlantic), indicating a positive correlation between the amplitude of the high frequency signal and **SWH**. However, **SWH** is not the only factor influencing the magnitude of the ionospheric high frequency signal. Indeed, high values of variance are also found within the tropical latitudinal band where **SWH** values are low. Given their location, these higher values can be for the moment hypothesised to be associated with scintillations and/or intense rain events. However, further analysis to assess their origin and potential impact will have to be included in future studies aiming at further optimizing the performance of the ionospheric correction.

Since our current results show that the high frequency components are characterized by null mean and constant standard deviation in time, it is reasonable to assume that they are due almost entirely to the stochastic error/noise in the measurements of ionospheric correction. Thus, they represent the signal to remove in order to improve the quality of the correction and to obtain more precise **SLA** products.

**Summary:** The dual-frequency ionospheric correction is directly proportional to the ionospheric TEC which is primarily controlled by solar radiation. Thus, the spatial distribution and temporal variability of the correction are function of three main factors:

- **Solar activity:** values of the correction increase during periods of stronger solar activity
- **Local time:** values of the correction are higher during local day times (maximum values around local 14:00) and lower during local night times (minimum values around local 2:00)
- **Latitudinal location:** correction values are highest within the tropics (maxima at around  $\pm 15^\circ$  of latitude) and smallest at high latitudes

Applying the raw ionospheric correction improves **SLA** observations when the correction values are large. However, the raw correction becomes ineffective (if not even detrimental) when the values are small.

High frequency variations of ionospheric correction are almost entirely due to errors associated with the measurement. Such **stochastic noise have to be filtered out** from the correction in order to improve the overall quality of the final **SLA** products.

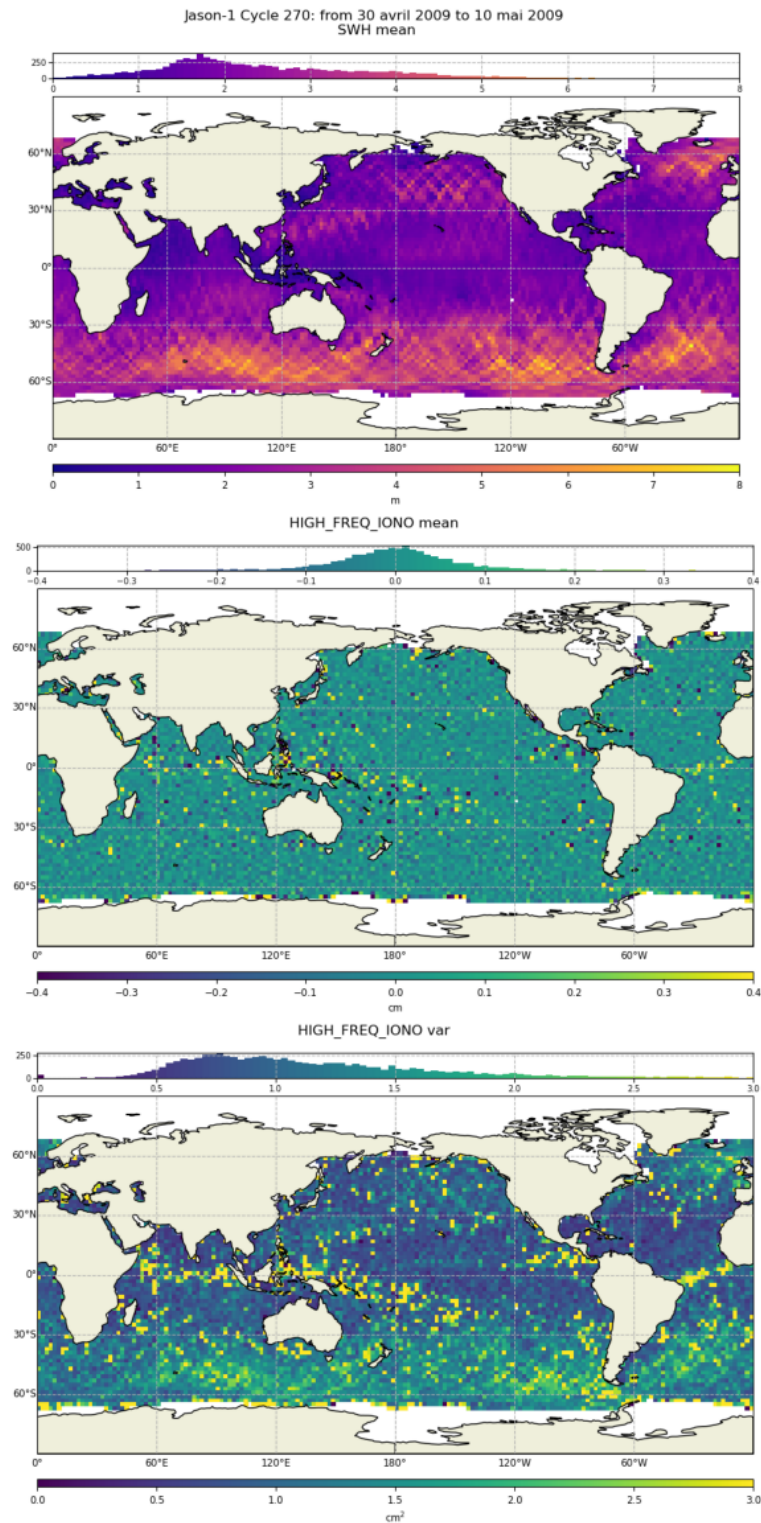


Figure 11 – Maps of *SWH* (top) and high frequency component of the ionospheric correction (middle) from Jason1 cycle 270 (from 30 April to 10 May 2009). Observations are averaged over 2° by 2° areas. The variance of the ionospheric high frequency component is shown in the bottom panel.

## 3. The Iterative Filter Method

The iterative filtering of the dual-frequency ionospheric correction adopted for the production of Sentinel-3 and Jason-3 GDR-F altimetry products is an evolution of the simple  $\mathcal{O}(200)$  km filtering originally proposed by [2] and [3] based on TOPEX observations. The new iterative filtering scheme was developed to achieve two main goals:

1. Provide a correction based on as many dual-band ionospheric observations as possible
2. Improve the correction for areas where altimetric observations are discontinuous or isolated (i.e. ice coverage, coastal areas, rain events . . .).

To achieve the first goal, the editing (i.e. selection of valid measurements) of the iterative filtering scheme is based on the quality of the measurements from the two altimetric bands, and independent on the SSH editing. While such decision results in a larger number of observations included in the computation of the ionospheric correction (i.e. in regions of strong precipitation, see Section 4.2.), it also introduces much more potential outliers in the analysis (as already observed in the example from Figure 1). To maximize the accuracy of the correction, such outliers have to be identified and removed from the analysis. An identification based on a single absolute threshold has revealed ineffective in the past, since the range of valid values characterizing the ionospheric correction can vary substantially depending on solar activity, local time and latitude location of a given observation (Sections 2.1. and 2.2.). Therefore, this new filtering scheme adopted an iterative procedure in which at each iteration a series of filters are applied to identify potential outliers based on thresholds defined on the measured variability of the observations, instead.

To achieve the second goal, a spline interpolation has been included as a last step of the analysis to fill the gaps in the filtered correction. This decision was based on the fact that the filtered correction varies slowly along the satellite track (i.e. long along-track correlation distance) and, thus, it can be accurately interpolated over distances of few hundreds km.

A detailed description of each step of the iterative filtering scheme is provided in the next Section 3.1.. The specific values of each parameter used for the production of Sentinel-3 and Jason-3 GRD-F products will be provided in Section 3.2..

### 3.1. Algorithm description

Figure 12 shows a flow chart with all the main steps included in the iterative filtering scheme. Light blue boxes and diamond indicate operations (i.e. filtering and interpolation) that requires parameters to be defined (these are all listed in Table 1); violet boxes indicate operations that do not require parameters (i.e. flagging, removal and writing).

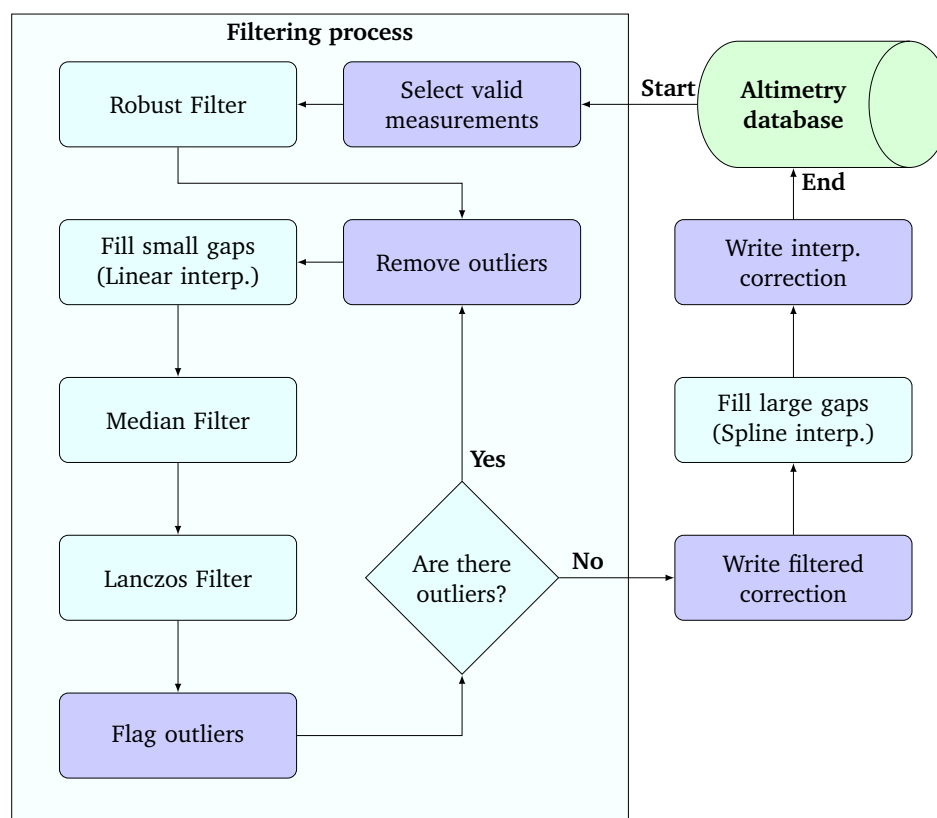


Figure 12 – Flowchart of the dual-frequency ionospheric correction filtering scheme

1. **Select valid measurements:** the first step of the filtering process is the selection of the observations to be used for the analysis (Figure 13, top). This process is referred to as “**editing**”. The selection is based on variables available from the Jason-3 and/or Sentinel-3 L2 products:

- Ionospheric correction  
(J3 GDR-F data01/ku/iono\_corr\_alt; S3 variable iono\_cor\_alt\_01\_ku)
- Surface type flag  
(J3 GDR-F data01/surface\_classification\_flag; S3 variable surf\_type\_01)
- Open sea-ice flag  
(J3 GDR-F data01/ice\_flag; S3 open\_sea\_ice\_flag\_01\_ku)
- Root Mean Square (RMS) of the “ocean” altimeter range  
(J3 GDR-F data01/ku/range\_ocean\_rms; S3 range\_ocean\_rms\_01\_ku)
- Number of valid points used to compute the “ocean” altimeter range  
(J3 GDR-F data01/ku/range\_ocean\_numval; S3 range\_ocean\_numval\_01\_ku)

Only measurements collected *a)* over the ocean, *b)* not on ice, *c)* for which the range at 1 Hz was computed with enough valid range observations at 20 Hz (RMS below a threshold 0.2 and a number of 20 Hz observations above a threshold of 10) and *d)* for which the ionospheric correction could be computed using equation 1 (its values different than Default Value (DV)) are selected.

It is important to note that the surface and ice flags are slightly different between the Jason-3 and Sentinel-3 missions. Jason-3 observations can be selected only over open oceans/semi-enclosed basins (data01/surface\_classification\_flag=0) and over no ice (data01/ice\_flag=0). Sentinel-3 ob-

.....

servations can be selected over open oceans/semi-enclosed basins or enclosed seas/lakes (surf\_type\_01=0 or 1, respectively) and over no ice or where the ice flag is not evaluated (open\_sea\_ice\_flag\_01\_ku=0 or 5, respectively).

The complete editing expressions for J3 is thus

```
data01/ku/iono_corr_alt!=DV &&
data01/surface_classification_flag==0 &&
data01/ice_flag==0 &&
(data01/ku/range_ocean_rms>0 && data01/ku/range_ocean_rms<0.2) &&
data01/ku/range_ocean_numval>10
```

The complete editing expressions for S3 is

```
iono_cor_alt_01_ku!=DV &&
(surf_type_01==0 || surf_type_01==1) &&
(open_sea_ice_flag_01_ku==0 || open_sea_ice_flag_01_ku==5) &&
(range_ocean_rms_01_ku>0 && range_ocean_rms_01_ku<0.2) &&
range_ocean_numval_01_ku>10
```

2. **Robust Filter:** After the valid measurements are selected a first filter can be applied to the measurements to remove the largest outliers. The filter simply computes the global average and standard deviation for the full series of measurements. The individual measurements for which the difference from the mean is INIT\_SIGMA times larger than the global standard deviation are flagged as initial large outliers. Currently this filter is activated and INIT\_SIGMA value is set to 5 in the prototype used to compute analysis on Jason-1 (further in this report), but not in that for Jason-3 GDR-F processing chain nor Sentinel-3 (see Table 1).

After the initial outliers are flagged, the filtering process enters the **iterative part of the scheme**: steps 3 to 7 are repeated until a condition on the minimum number of allowed outliers is met. At each iteration, the filter is applied to all raw corrections not flagged as outliers.

3. **Remove outliers:** raw measurements flagged as outliers are removed from the analysis (red curve in Figure 13, middle).
4. **Fill small gaps:** small gaps between raw measurements can be filled through linear interpolation. The variable DATA\_GAP\_MAX defines the maximum size (in number of points) above which a gap should not be filled through linear interpolation. If the variable is set to 0, then no filling is performed and the step is entirely skipped by the analysis. This is the current setting for both Jason-3 GDR-F and Sentinel-3 processing chains.
5. **Median Filter:** a median filter is applied to further remove local outliers. This results in a strong reduction of the correction noise (blue curve in Figure 13). The variable MEDIAN\_NB\_PTS defines the half-width (in number of points) of the filter window. MEDIAN\_NB\_PTS\_MIN defines the minimum number of valid points within the window to apply the filter (the filtered value is flagged as invalid otherwise). The filter can be applied with or without averaging depending on the MEDIAN\_NB\_PTS\_MEAN variable. If set to 0 (as it is currently the case for Jason-3 GDR-F and Sentinel-3 processing chains), then the filter is applied without averaging (i.e. for any observation it returns the median value within the window centered around that observation); however, if MEDIAN\_NB\_PTS\_MEAN > 0, the filter is applied with averaging (i.e. for any observation it returns the average value of MEDIAN\_NB\_PTS\_MEAN number of observations centered around the median value).

- .....
6. **Lanczos Filter:** a low-pass Lanczos filter is applied to smooth the median filtered correction and further reduce its noise. The Lanczos filter was chosen because one of many practical (finitely supported) approximations of the sinc filter. As such, it is particularly effective at removing frequency (or, as in our case, wavenumbers) components above a given cutoff frequency, without affecting lower frequencies. Its kernel is defined as a sinc filter multiplied (modulated) by the Lanczos window [5]. The variable LANCZOS\_NB\_PTS determines the half-width of the Lanczos kernel. LANCZOS\_NB\_PTS\_CUTOFF determines the filter cutoff length (the resulting cutoff wavenumber is simply  $\text{LANCZOS\_NB\_PTS\_CUTOFF}^{-1}$ ), and hence the shape of the Lanczos kernel within the filter window. When LANCZOS\_NB\_PTS\_CUTOFF have the same length as LANCZOS\_NB\_PTS (as in the case of both Jason-3 GDR-F and Sentinel-3), the kernel will have two zero-crossings within the given window (the so called Lanczos-2 kernel). Each filtered value is the weighted sum of  $2 \times \text{LANCZOS\_NB\_PTS}$  consecutive input samples around a given observations. As for the median filter, LANCZOS\_NB\_PTS\_MIN defines the minimum number of valid points within such window to apply the filter (the filtered value is flagged as invalid otherwise).
  7. **Flag outliers:** After the filtered correction is computed, the differences between each filtered correction and the raw correction are computed. Individual raw corrections are flagged as outliers if their difference from the filtered correction is more than 3 times larger than the standard deviation of the global difference distribution.
  8. **Are there outliers?:** steps 3 to 7 are repeated until the percentage of remaining outliers within the raw measurements of ionospheric correction equals or drops below a given threshold. Such threshold is defined by the variable CONVERGENCE\_THRESHOLD. In this report, a convergence threshold is set to 0.1% in case of prototype used for Jason-1 analysis, whereas no outlier is authorized for Jason-3 or Sentinel-3 processing chains (convergence threshold = 0).

When the condition “percentage of remaining outliers  $\leq$  CONVERGENCE\_THRESHOLD” is met, the iterative filtering stops, and the processing enters the last portion of the scheme, where eventual gaps in the correction are filled.

9. **Write filtered correction:** as intermediate step, all valid values of the filtered correction are saved on the altimetry database.
10. **Fill large gaps:** gaps in the filtered correction are filled using a Spline interpolation. Due to the large along-track correlation distance of the filtered ionospheric correction, this interpolation is used to fill gaps up to the order of few hundreds of km. The variable NB\_PTS\_INTERP\_SPLINE defines the half-width of the Spline interpolation windows (i.e. how many valid points at the beginning and the end of the gap are used for the interpolation). DISTANCE defines the maximum allowed distance between the interpolated point and each of the extremities of the interpolation windows.
11. **Write interp. correction:** As a last step of the iterative filtering scheme, the filtered and interpolated correction is saved on the altimetry database (Figure 13, bottom).

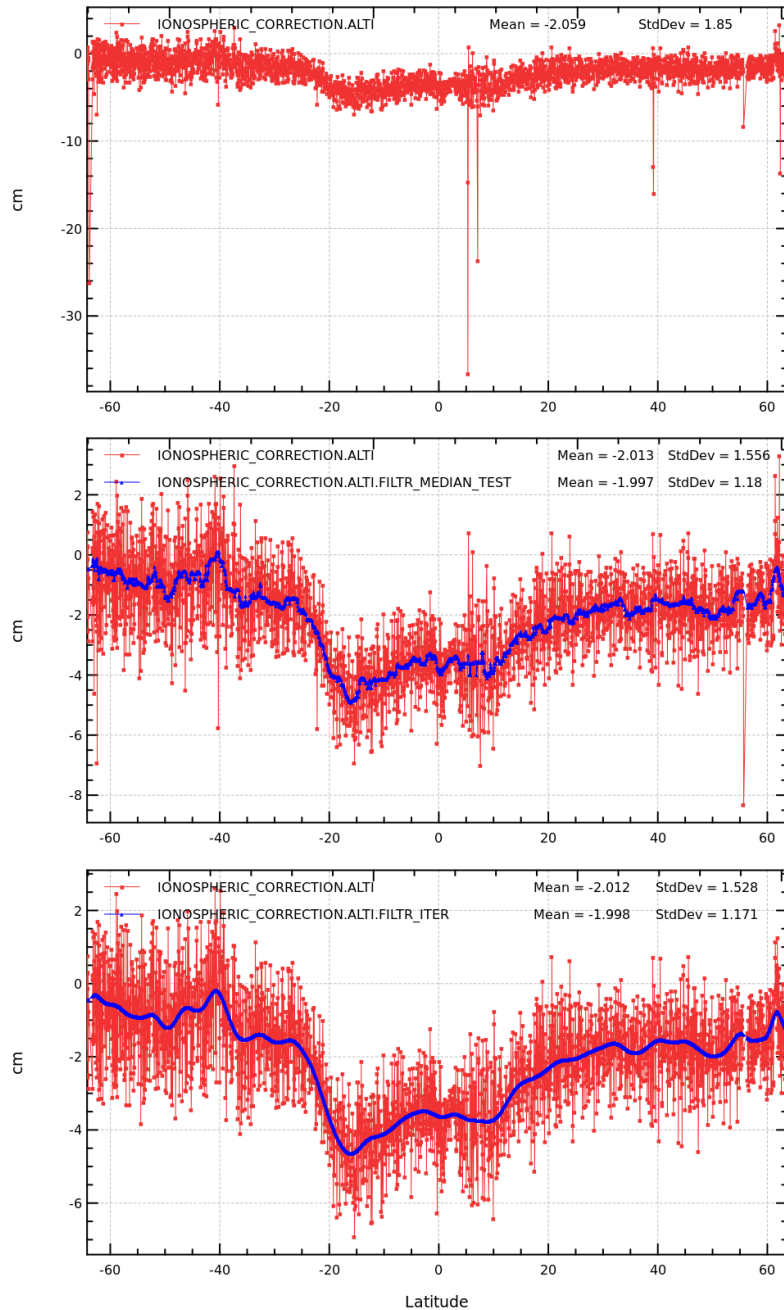


Figure 13 – Evolution of the dual-frequency ionospheric correction at different steps of the iterative filtering scheme for Jason-1 track 004 from cycle 280. (Top) All valid measurements selected after step 1. (Middle) Valid measurements retained after the robust filter is applied (red) and resulting median filtered correction (blue) at the end of step 5 for the first iteration. (Bottom) Final filtered and interpolated correction (blue) at the end of step 11 and all valid raw observations used to compute it (red). Note that the y-axis limits change between figures as outliers are progressively removed through the iterative filtering.

Step	Variable	(Units)	Values	
			Jason-3 GDR-F	Sentinel-3
<b>2. Robust Filter</b>	INIT_SIGMA	(-)	None	None
<b>4. Fill small gaps</b>	DATA_GAP_MAX	(pts)	0	0
<b>5. Median Filter</b>	MEDIAN_NB_PTS	(pts)	20	20
	MEDIAN_NB_PTS_MIN	(pts)	10	5
	MEDIAN_NB_PTS_MEAN	(pts)	0	0
<b>6. Lanczos Filter</b>	LANCZOS_NB_PTS	(pts)	50	50
	LANCZOS_NB_PTS_CUTOFF	(pts)	50	50
	LANCZOS_NB_PTS_MIN	(pts)	10	5
<b>8. Are there outliers?</b>	CONVERGENCE_THRESHOLD	(%)	0	0
<b>10. Fill large gaps</b>	NB_PTS_INTERP_SPLINE	(pts)	20	20
	DISTANCE	(km)	500	250

Table 1 – Values of each variable used at different steps of the iterative filtering scheme for the production of Jason-3 GDR-F and Sentinel-3 products.

### 3.2. Jason-3 and Sentinel-3 specifications

Table 1 lists the values for the parameters described in Section 3.1. used to derive Jason-3 GDR-F and Sentinel-3 products. Justification for some of the adopted values are discussed in Chapter 5.

**Summary:** The iterative filtering scheme was developed to achieve two main goals:

- Base the correction on as many dual-band ionospheric observations as possible
- Improve the correction where altimetric observations are discontinuous or isolated.

Selection of the ionospheric observations used for the correction is independent from the quality of sea level observations. This maximizes the number of observations selected, but at the same time increases the number of potential outliers.

The iterative filtering applies a median and a Lanczos filter in sequence, in order to progressively reduce the number of outliers in the ionospheric observations used to compute the final filtered correction.

Since the filtered correction has long spatial correlation scales, a spline interpolation is used to fill gaps in the interpolated correction up to few hundreds km.

## 4. Evaluation of the iterative filtering on Jason-3 GDR-F observations

To assess the performance of the iterative filtering, we analyse two diagnostics:

- the *SLA* variance reduction (as in Section 2.3.)
- the number of along-track observations without an associated ionospheric correction

The analysis is based on Jason-3 observations spanning from cycle 17 to 58 (from 25 July 2016 to 14 September 2017), since at the time of this analysis they are the cycles reprocessed according to the latest GDR-F standards (and thus include the iterative filtered ionospheric correction). In the next sections, results obtained using the iterative filtered dual-frequency ionospheric correction are compared to the ones obtained using the raw correction.

The same analysis was also performed on Sentinel-3A 1Hz SAR and PLRM observations from cycles 7 to 21, covering the same period as the Jason-3 observations. Results were analogous to those from Jason-3. Figures from Sentinel-3A SAR observations are included in Appendix A. and the end of this document.

### 4.1. Explained *SLA* with respect to raw correction

Following [3], the explained variance ( $\Delta VAR_{SLA}$ ) and the percentage of explained variance ( $\% VAR_{SLA}$ ) are used to compare the different impact of the raw and the iterative-filtered correction on the final *SLA*. The two variables are defined according to equations 2 and 3 provided in Section 2.3..

#### 4.1.1. Spatial distribution

Figure 14 shows the distribution of  $\Delta VAR_{SLA}$  and  $\% VAR_{SLA}$  computed using the raw ionospheric correction and averaged over areas of  $2^\circ$  by  $2^\circ$  for the whole period of investigation. The figure is analogous to Figure 8 derived using Jason-1 observations over 2009, and shows similar patterns: the raw ionospheric correction improves *SLA* observations within the tropics (positive values for both  $\Delta VAR_{SLA}$  and  $\% VAR_{SLA}$ , indicating a reduction in *SLA* variance) but degrades the observations at higher latitudes. The relative impact of the correction (either positive or negative) is larger away of the highly energetic ocean regions (western boundary currents, Agulhas region and Antarctic Circumpolar Current). The similarities between Figure 14 and Figure 8 should not be surprising, since (as shown by Figure 3) the observations for both figures spans periods characterized by similar levels of solar activity resulting in analogous values of ionospheric correction.

Histograms of the global values of  $\Delta VAR_{SLA}$  and  $\% VAR_{SLA}$  are shown above each maps in Figure 14. They both indicate that the regions where the raw correction improves the final *SLA* observations represent a minor portion of the total, whereas the *SLA* variance increases after the correction is applied (i.e. negative values of  $\Delta VAR_{SLA}$  and  $\% VAR_{SLA}$ ) over the majority of the world oceans. Overall, the global average and median values of  $\Delta VAR_{SLA}$  using the raw correction are  $-2.4$  and  $-2.3$   $\text{cm}^2$ , respectively.

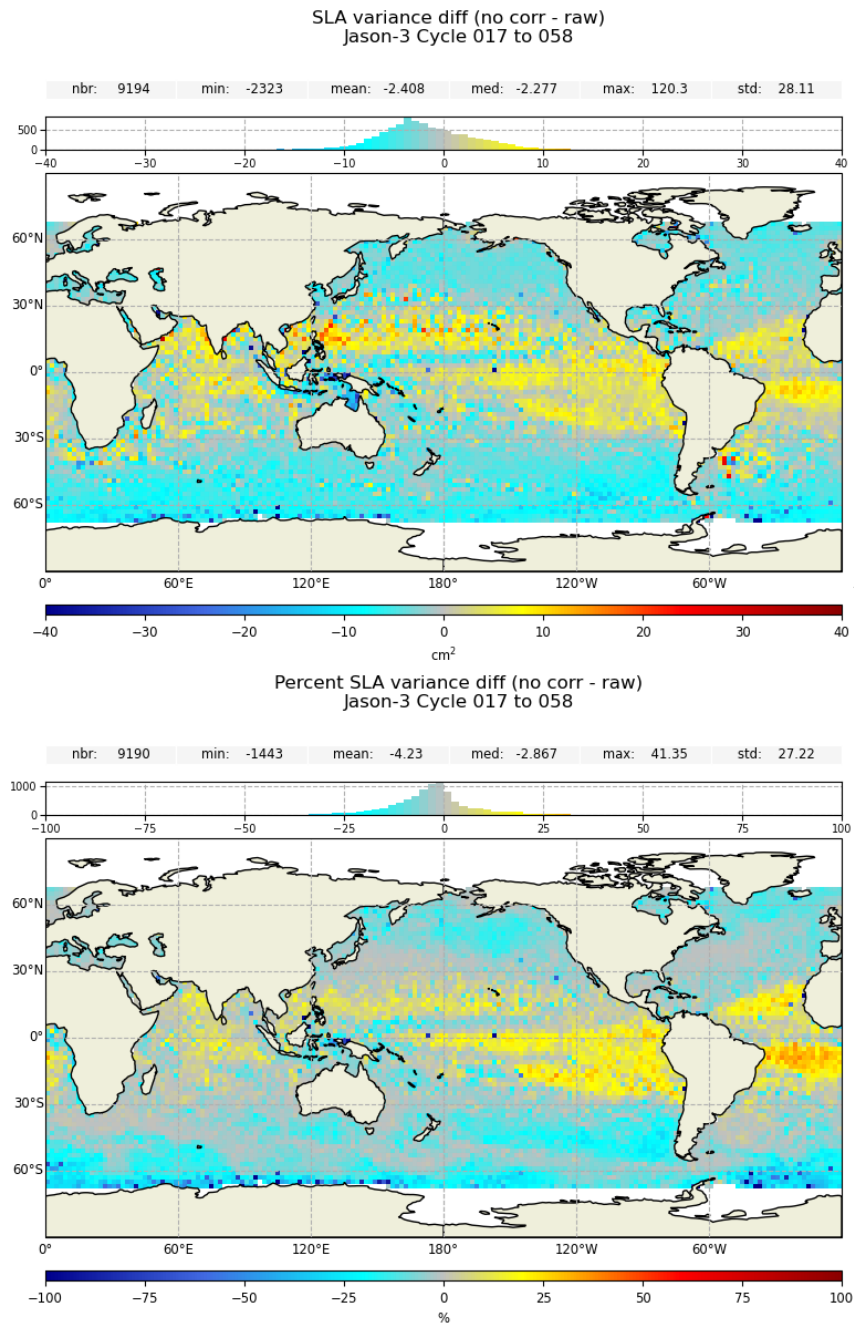


Figure 14 – Maps of of variance difference (top) and percentage of variance difference (bottom) between the SLA computed without correction and that computed using the raw correction using Jason-3 observations from cycle 17 to cycle 58. In both maps, satellite observations are averaged over 2° by 2° areas.

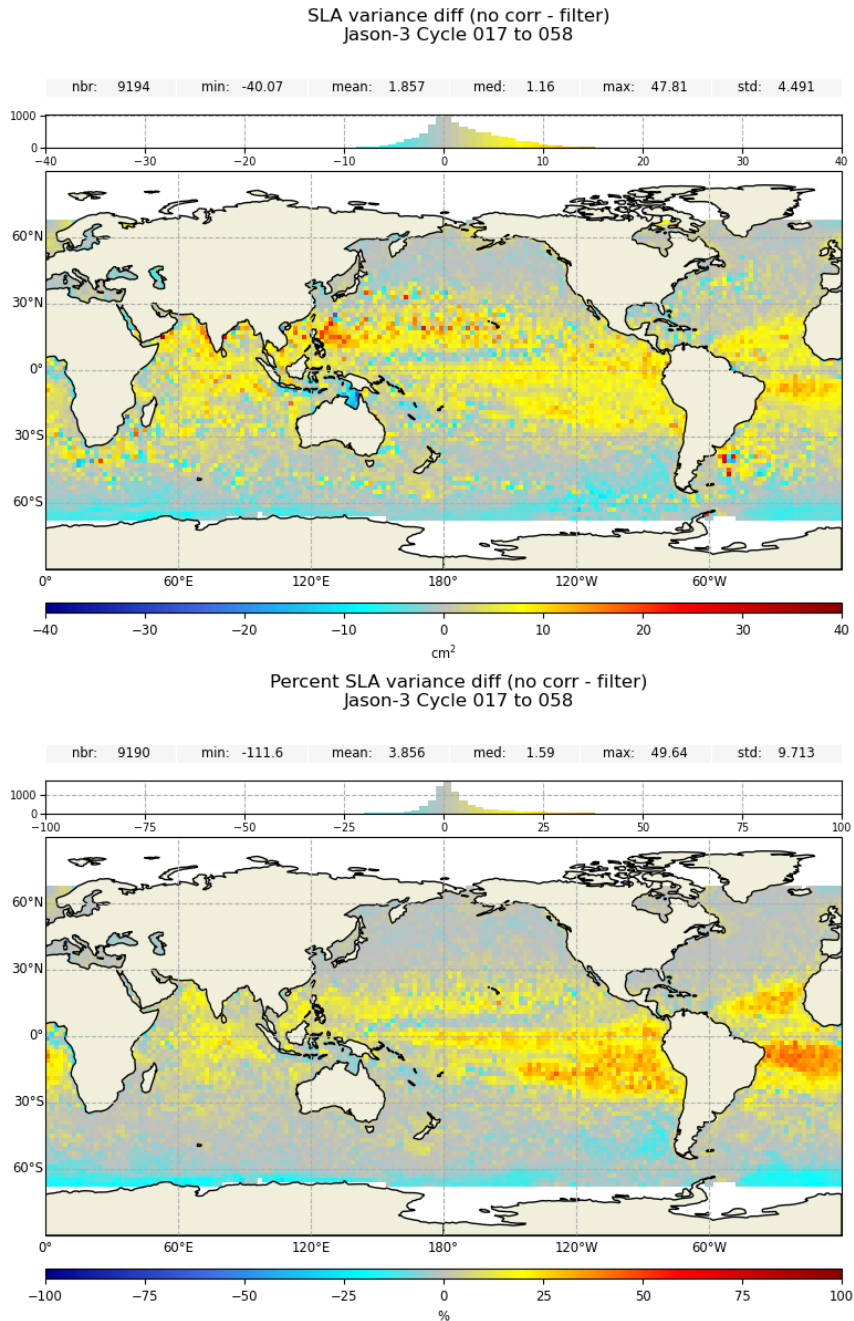


Figure 15 – Same as figure 14, but using the iterative filtered correction instead.

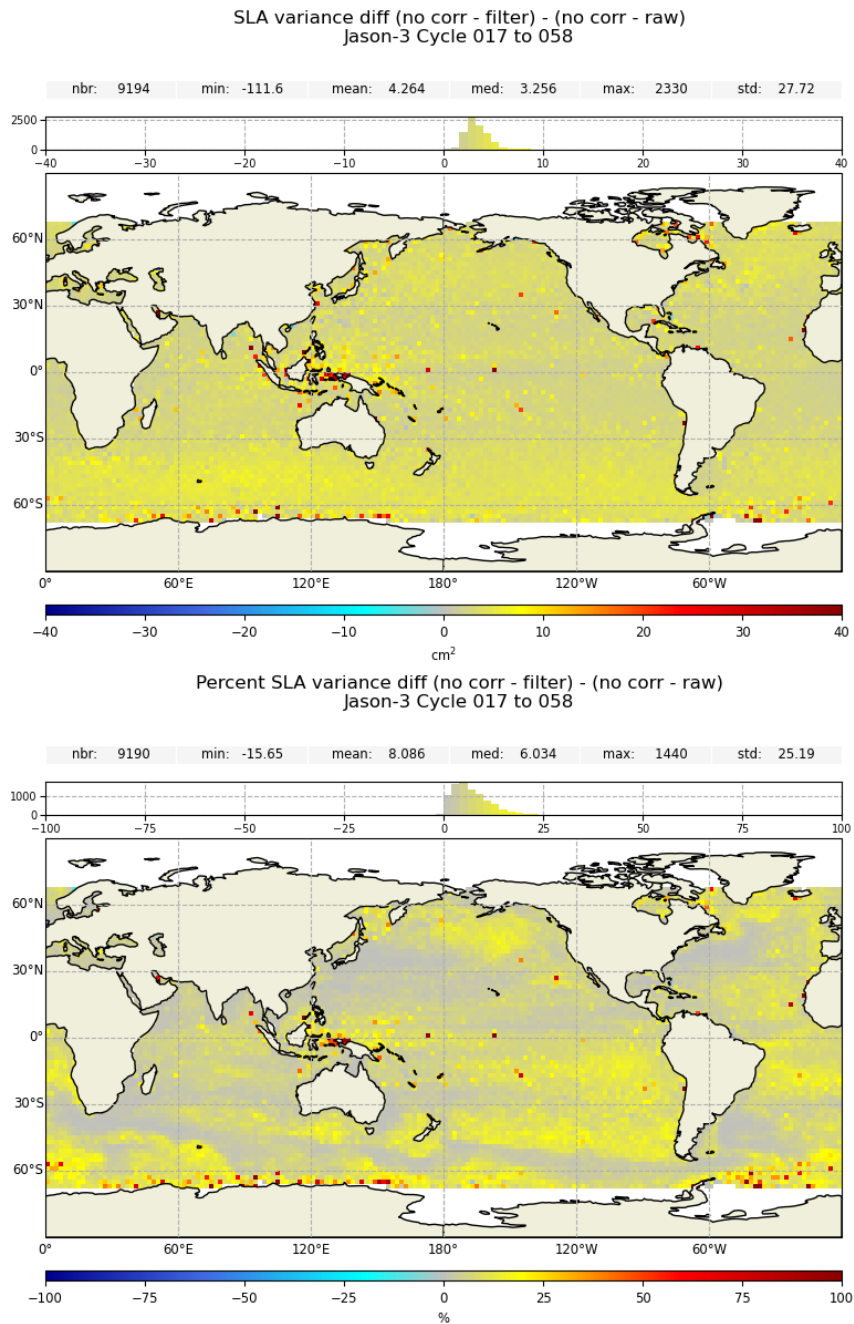


Figure 16 – (Top) Maps of the difference between  $\Delta VAR_{SLA}$  computed using the iterative filtered ionospheric correction (Figure 15, top) and that computed using the raw correction (Figure 14, top). (Bottom) Same as top panel, but for %  $VAR_{SLA}$ . In both maps, satellite observations are averaged over  $2^\circ$  by  $2^\circ$  areas.

Figure 15 shows analogous maps as Figure 14, but computed using the filtered ionospheric correction instead. Positive values of the two variables show spatial patterns are similar to those observed in Figure 14 but are characterized by larger values. Regions of negative values are largely reduced. This is confirmed also by the global histograms of the two variables, which show distributions with mode centered around 0 and skewed toward positive values (i.e. longer tails of positive value compared to the negative ones). The fact that regions of negative values persist also when the filtered correction is applied suggest that some aspects in the current filter design and parametrization (e.g. cutoff wavelength) are not yet optimised. Thus, they could be further improved with dedicated sensitivity studies in order to maximize the filter performance. Overall average and median of  $\Delta VAR_{SLA}$  using the iterative filtered correction are +1.9 and +1.2 cm<sup>2</sup>, respectively. Thus, at the global scale the iterative filtered correction improves SLA observations.

This can be better visualized from Figure 16, which shows the difference between  $\Delta VAR_{SLA}$  and % $VAR_{SLA}$  computed using the iterative filtered correction and those computed using the raw correction. The two maps and the corresponding histograms show predominantly positive values, indicating that the iterative filtered correction outperforms the raw correction pretty much everywhere. Within the tropics, where values of  $\Delta VAR_{SLA}$  and % $VAR_{SLA}$  based on the raw correction are already positive, the iterative correction further improves SLA observations. On the other hand, at low latitudes, where the raw correction introduces additional variance to SLA observations, the iterative filtered correction does not degrade them. Overall, the average and median further reduction of  $\Delta VAR_{SLA}$  associated with the iterative filtered correction with respect to the raw correction are +4.3 and +3.3 cm<sup>2</sup>, respectively.

#### 4.1.2. Temporal variability

A complementary approach to compare the performances of the two types of correction is to investigate how they vary with time. Figure 17 shows the time series of the average SLA variance per cycle for the SLA computed without any ionospheric correction (blue line), for that computed using the raw dual-frequency ionospheric correction (red line) and for that computed using the iterative filtered correction (cyan line) for Jason-3 GDR-F observations from cycles 17 to 58. The figure confirms that, on average, the raw correction improves SLA observations (raw curve below the blue one) only at times when the ionospheric correction signal is strong (Oct-Nov 2017). When the correction signal is weak, then the raw correction introduces additional variance, thus degrading the SLA observations. On the other hand, the iterative filtered correction further decrease the SLA variance when the correction signal is strong, and maintains similar values as the uncorrected SLA when the correction signal is weaker.

This can be further investigated analysing analogous time series, but from the full Jason-1 time series, which, compared to Jason-3 cycles 17 to 58, spans a broader range of solar activity levels and, hence, of ionospheric correction values (see Section 2.1.1.). The three time series in Figure 18 show that during years of strong solar activity (2002 to 2005 and 2012), raw and iterative filtered corrections can be both successfully applied to significantly reduce SLA variance. Nonetheless, the iterative filtered correction always outperforms the raw correction, since it induces a slightly larger reduction in SLA variance (of the order of few cm<sup>2</sup>). This becomes particularly important in years of weak solar activity (2007 to 2010) when the raw correction becomes ineffective at reducing SLA variance (and in some cases becomes even detrimental by increasing it), whereas the iterative filtered correction remains effective (although the reduction is of a significantly smaller proportion than observed during years of strong solar activity).

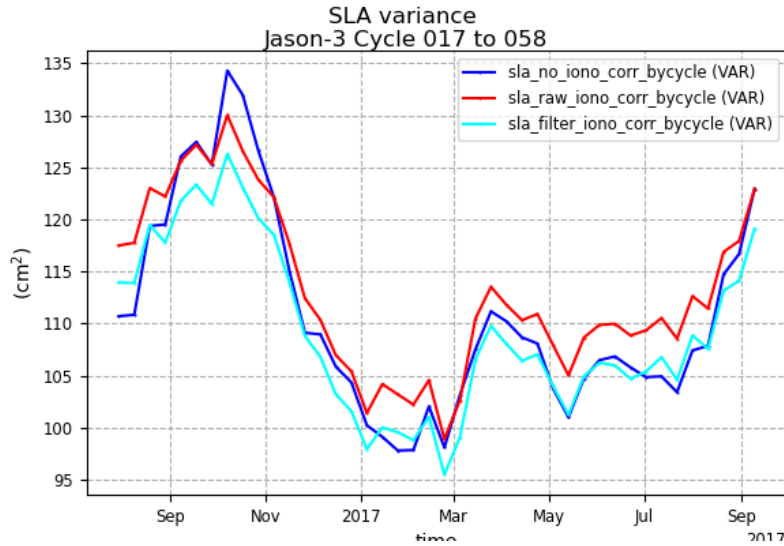


Figure 17 – Time series of the average SLA variance per cycle for Jason-3 observations from cycles 17 (2016/08) to 58 (2017/09). *Blue curve is for SLA without any ionospheric correction; red curve is for SLA with the raw ionospheric correction; cyan curve is for SLA with the iterative filtered ionospheric correction.*

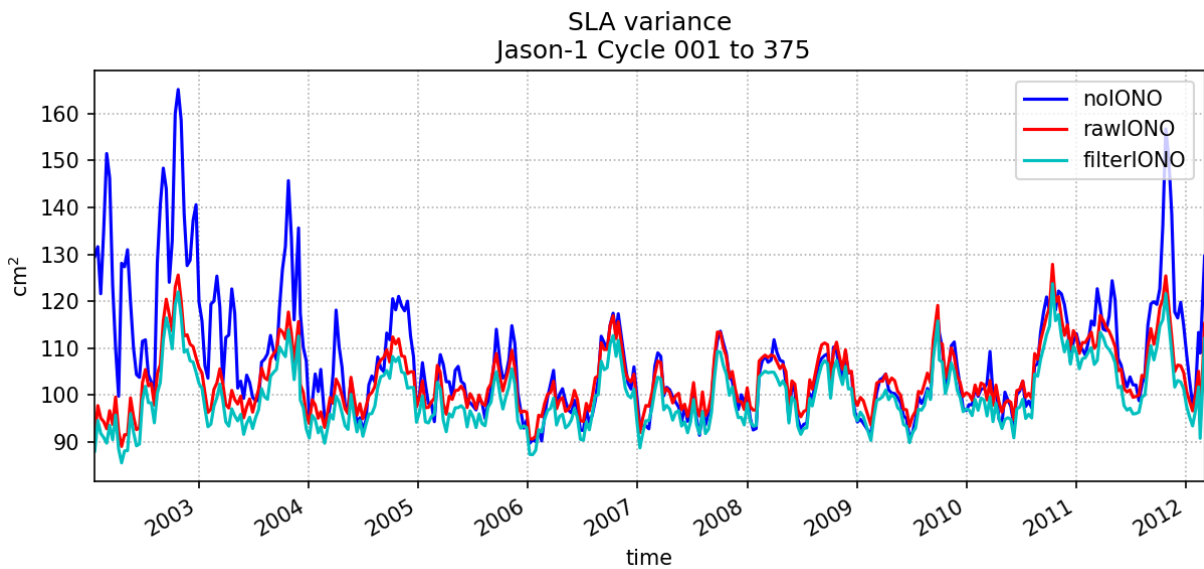


Figure 18 – Same as Figure 17, but for the full Jason-1 time series (cycles 1 to 375). *Blue curve is for SLA without any ionospheric correction; red curve is for SLA with the raw ionospheric correction; cyan curve is for SLA with the iterative filtered ionospheric correction.*

---

## 4.2. Number of points edited by the algorithm

---

A second expected advantage of the iterative filtering approach is to improve the ionospheric correction in regions where altimetric observations are discontinuous or isolated (due for instance to ice coverage, coastal areas or rain events). To assess this aspect, we investigated how the total number of edited points (i.e. flagged with invalid/missing value of ionospheric correction) and their spatial distribution varies between the raw and iterative filtered ionospheric correction. In the iterative filtered correction, these points correspond to the ones for which a Lanczos filtered value could not be computed (because the number of valid points within the filtering window  $< \text{LANCZOS\_NB\_PTS\_MIN}$ ) and that subsequently could not be filled via Spline interpolation (because their distance from at least one of the two extremities of the interpolation window  $> \text{DISTANCE}$ ; see Section 3.1.). The analysis was based on Jason-3 GDR-F observations from cycle 020, collected at the end of 2016 northern hemisphere summer (from August 23 to September 2). Only measurements over open ocean (i.e. not over land or ice) were included in the analysis.

Figure 19 shows the geographical distribution of points with edited ionospheric correction for both raw and iterative filtered corrections. Overall, the total number of points edited by the raw correction is 4414; that edited by the iterative filtered correction 5225. The majority points edited by the raw correction occurs in the open ocean and, thus, they are most likely associated with invalid ionospheric correction values due to intense rain events. Since those points are almost entirely edited by the raw correction only (**red circles; 2377 points total**), the iterative filtering is successful at retrieving ionospheric correction values under such events (either through the Lanczos filtering or the successive Spline interpolation). At the same time, a similar success is not observed for correction values along the coast: most of the points edited by the raw correction remain edited even in the case of the iterative filter one (**green circles; 2037 points total**). Moreover, the iterative filter correction substantially increases the number of edited points along the coast of the main continents (especially at high latitudes) and along the border of the Antarctic sea ice (**blue circles; 3188 points total**).

Such points are edited by the iterative filtered correction but not by the raw one, most likely due to the impossibility in those boundary regions to satisfy the conditions for the Lanczos filtering or the Spline interpolation required by the iterative filtered correction. While a detailed analysis of the filtered correction performance in the nearshore regions and along the ice margins was beyond the objectives of this technical note, these aspect will need to be addressed by future studies focusing on the further optimization of the iterative filter.

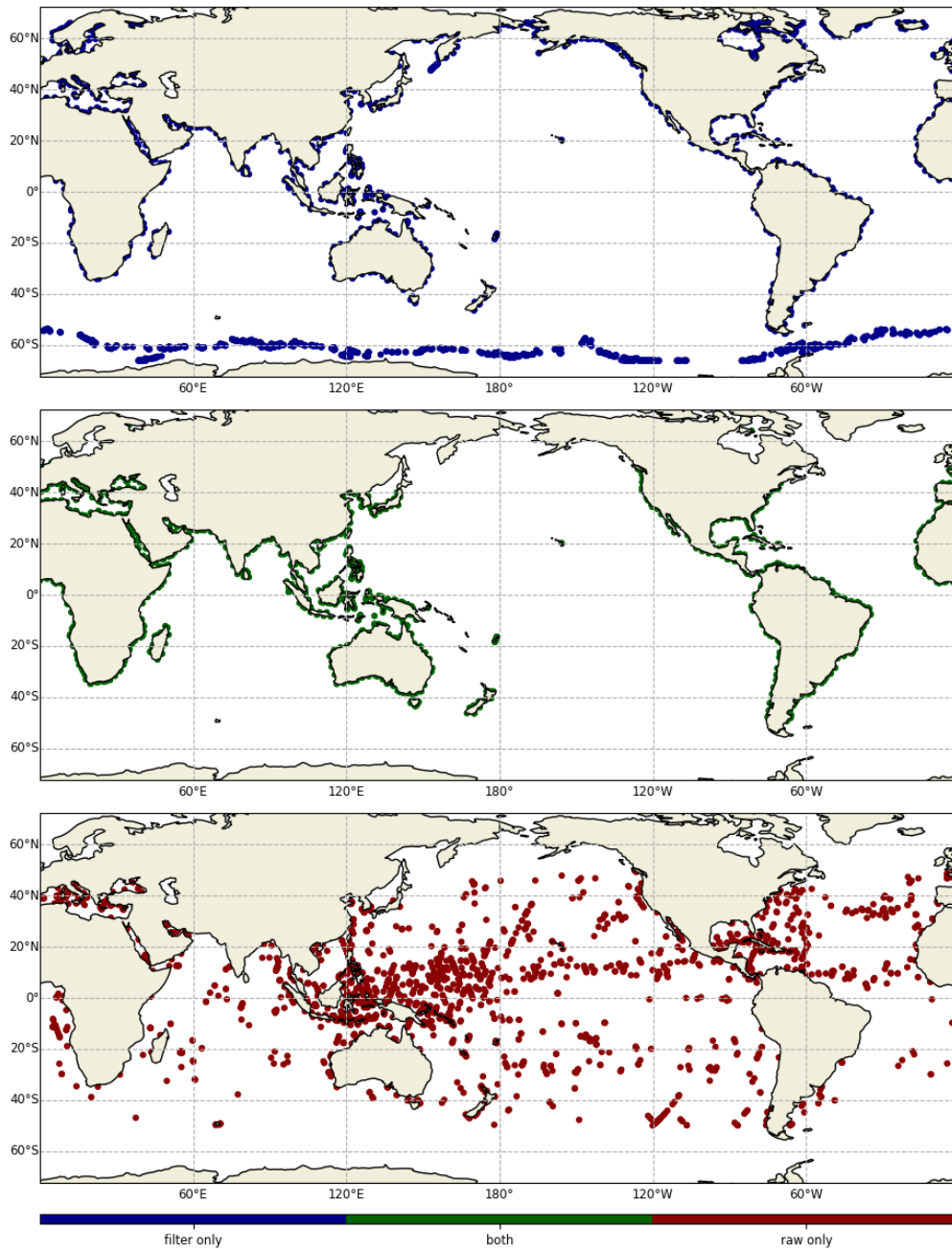


Figure 19 – Distribution of points with edited ionospheric correction for Jason-3 GDR-F observations from cycle 20. Blue circle are points edited only using the iterative filtered correction; red circles are points edited only using the raw filtered correction; green circles are edited points common to both corrections.

**Summary:** The SLA variance reduction from the iterative filtered ionospheric correction is always larger than that from the raw correction, regardless of the values of the correction. Thus, **the iterative filtered correction outperforms the raw correction over all ocean regions and for any level of solar activity:**

- Within the tropics and/or during years of strong solar activity (i.e. high correction value conditions), when the raw correction already reduces the variance of SLA observations, the iterative correction further improves them.
- At low latitudes and/or during years of weak solar activity (i.e. low correction value conditions), when the raw correction introduces additional variance to SLA observations, the iterative filtered correction can still improve (or at least not degrade) them.

Due to the use of the Lanczos filtering and Spline interpolation, the iterative filtered correction **increases the number of valid correction values in the open ocean regions** impacted by intense rain events.

On the other hand, the **number of edited values is substantially increased along the continental coast-lines and the Antarctic ice margins.**

## 5. Conclusions

This report provided a description of the iterative filtering method applied to the dual-frequency ionospheric correction to derive Sentinel-3 and Jason-3 GDR-F altimetry products. This correction is measured from two different frequency bands ( $K_u$  and  $C$ ) and, thus, is inherently noisy since it includes measurements errors from both bands as well as errors associated with the choice of the **SSB** correction applied to those measurements. Furthermore, as the correction is directly proportional to the ionospheric **TEC** (which in turn is primarily controlled by solar radiation) it is also characterized by large spatio-temporal variability. Temporally, its values increase during periods of strong solar activity and are highest during day time. Spatially, they are highest within the tropics and smallest at low latitudes.

Directly applying the noisy raw ionospheric correction to altimetry observations improves the final **SLA** products (i.e. reducing their variance) when the correction values are high (due to a lower **SNR**). However, the raw correction becomes ineffective, and often detrimental (i.e. it increases **SLA** variance), when correction values are low (due to a higher **SNR**). Since the noise induced by the stochastic errors in the ionospheric measurements is almost entirely contained within the high-frequency component of the correction, a low-pass filter can be applied to remove it and, thus, enhance the effectiveness of the correction in improving the final **SLA** products.

The iterative filtering scheme described in the report was developed in order to a) base the correction on as many dual-band ionospheric observations as possible, and b) improve the correction where altimetric observations are discontinuous or isolated. To reach the first goal, the ionospheric observations used for the correction are selected independently from the quality of **SLA** observations. These observations are then filtered applying a median and a low-pass Lanczos filter in sequence. Since the new data selection can increase the number of potential outliers included in the analysis, the filters are applied multiple times iteratively in order to progressively identify and reduce the number of outliers used in the computation of the final filtered correction. As a last step, the second goal is achieved by applying a Spline interpolation at the end of the iterative process to fill any gap in the filtered correction up to few hundred kilometers (since the filtered correction is characterized by long spatial correlation scales).

Our analysis showed the iterative filtered ionospheric correction always results in a larger reduction of **SLA** variance than the raw correction, regardless of the values of the correction. Thus, **the iterative filtered correction outperforms the raw correction over all ocean regions and for any level of solar activity**. Furthermore, due to the use of the Lanczos filtering and Spline interpolation, the iterative filtered correction increases the number of valid correction values in the open ocean regions impacted by intense rain events. However, at the same time, the number of edited values is substantially increased along the continental coastlines and the Antarctic ice margins.

## Appendix A. Evaluation of the iterative filtering on Sentinel-3A observations

Analysis of the spatial and temporal variability of the explained variance analogous to that performed on Jason-3 observations in Section 4., was also performed on Sentinel-3A 1 Hz SAR and PLRM observations. The observations are from cycles 7 to 21, covering the same temporal period (i.e. from July 2016 to September 2017) as the ones from Jason-3.

Maps and time series from Sentinel-3A observations are shown in figures 20 to 23. They show analogous results as the ones discussed for Jason-3. Figure 20 shows the largest negative values within the high-latitude polar regions. These are not sampled by Jason-3, therefore a direct comparison cannot be performed. The reason why they occur remains unclear and will be the object of future studies specifically dedicated at assessing the performance of the filtered correction within the near-shore regions and along the ice margins. Such negative high-latitude patterns disappear once the filter is applied (figure 21) and hence correspond to regions a large improvement (i.e. large positive values) when performance of raw and filtered correction are compared (figure 22).

Compared to Jason-3 results, Sentinel-3A shows slightly worse performance, for both raw and filtered ionospheric correction, in the equatorial band of Pacific and Atlantic Oceans. The reasons why this occurs will be also investigated in future dedicated studies.

Finally, although not shown, results for Sentinel-3A PLRM observations are almost entirely analogous to the ones from SAR. The main difference consists in even worse performance of the raw correction across all ocean basins, with only very limited regions showing positive values of variance difference. Applying the filtered correction largely reduces such negative impact. Thus, although the overall performance of PLRM filtered correction is worse than the SAR one, the differences between raw and filtered PLRM correction is characterized by much larger values.

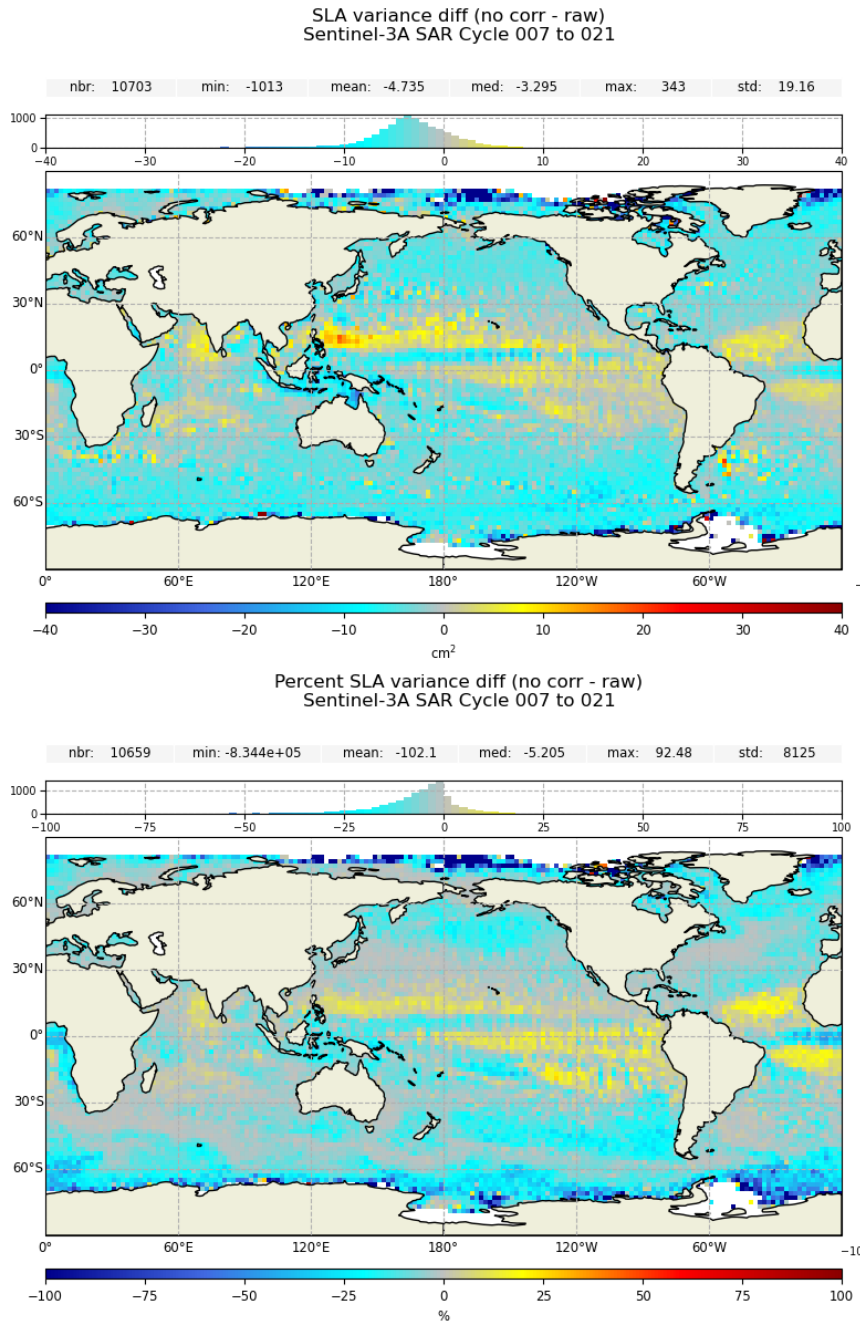


Figure 20 – Same as figure 14, but using Sentinel-3A SAR 1Hz observations. The observations are from cycles 7 to 21 covering the same period (2016/07 to 2017/09) as the Jason-3 data used in Section 4.

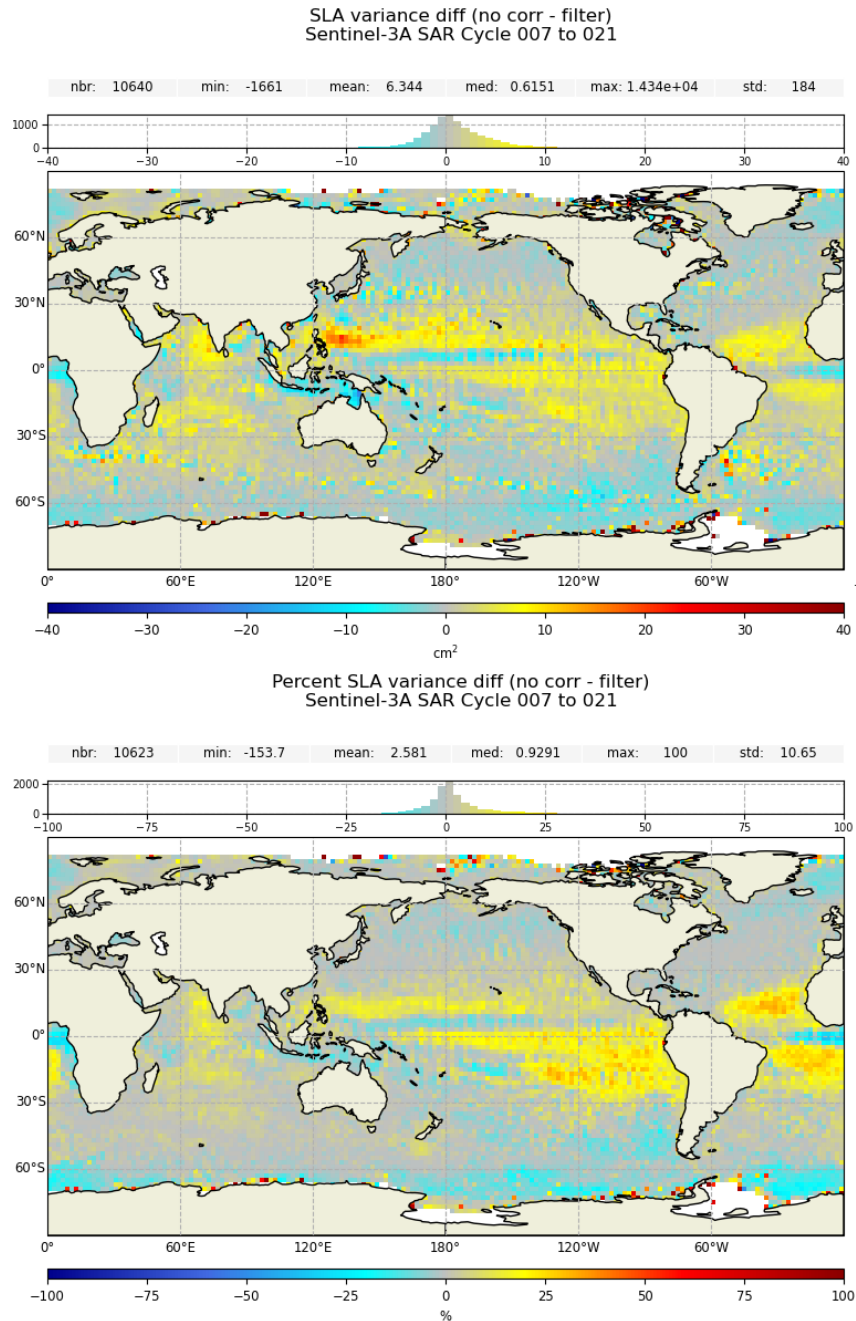


Figure 21 – Same as figure 20, but using the iterative filtered correction instead.

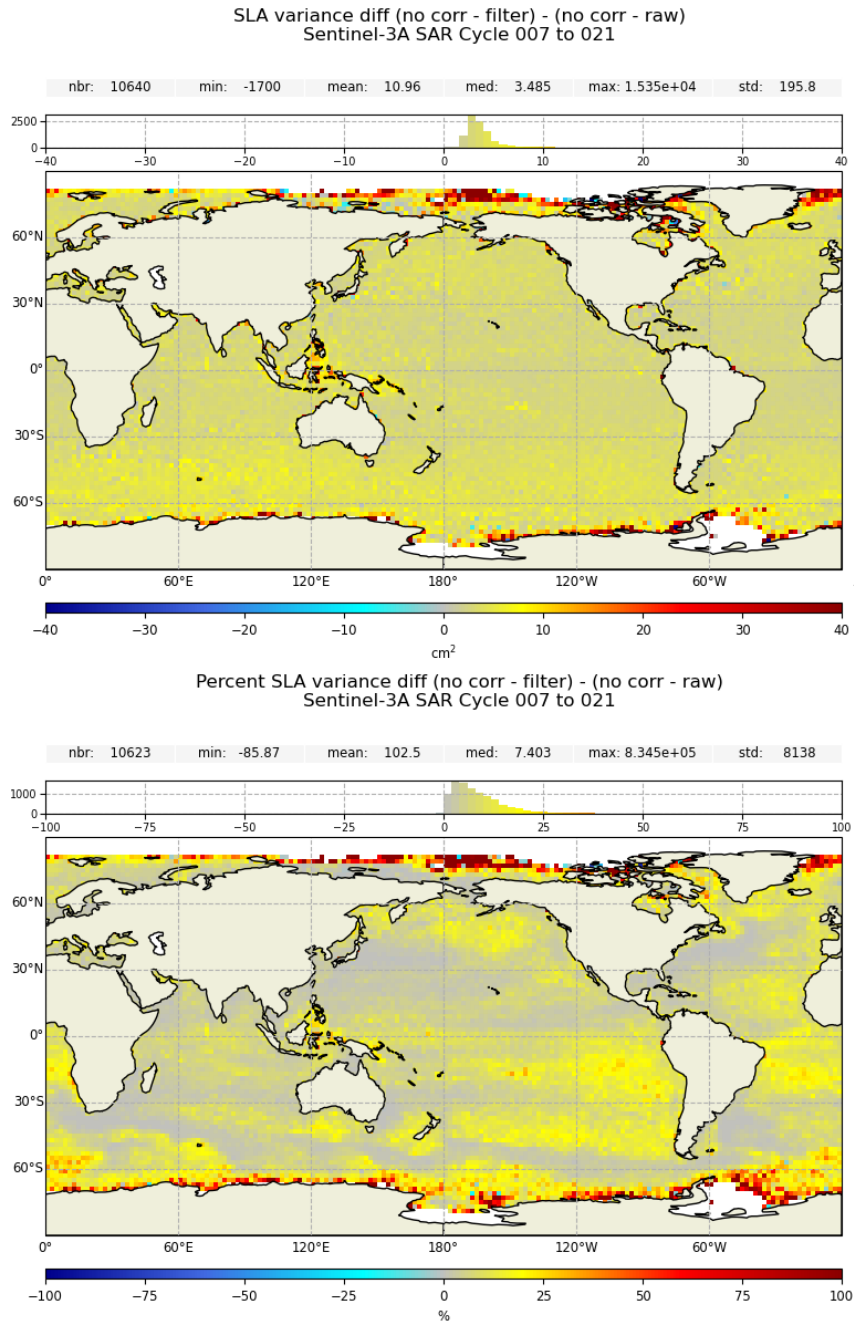


Figure 22 – Same as figure 16, but using Sentinel-3A SAR 1Hz observations as in figure 20.

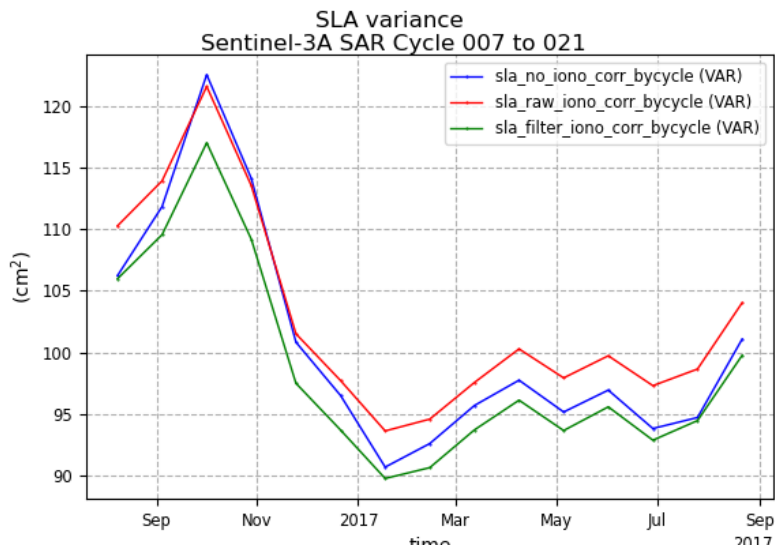


Figure 23 – Same as figure 17, but using Sentinel-3A SAR 1Hz observations as in figure 20. Blue curve is for SLA without any ionospheric correction; red curve is for SLA with the raw ionospheric correction; green curve is for SLA with the iterative filtered ionospheric correction.

## References

- [1] R. H. Stewart, *Methods of Satellite Oceanography*. University of California Press, 1985.
- [2] D. A. Imel, "Evaluation of the topex/poseidon dual-frequency ionosphere correction," *Journal of Geophysical Research*, vol. 99, NO. C12, pp. 24,895–24,906, 1994.
- [3] V. Zlotnicki, "Correlated environmental corrections in topex/poseidon, with a note on ionospheric accuracy," *Journal of Geophysical Research*, vol. 99, NO. C12, pp. 24,907–24,914, 1994.
- [4] J. L. Lean, R. R. Meier, J. M. Picone, F. Sassi, J. T. Emmert, and P. G. Richards, "Ionospheric total electron content: Spatial patterns of variability," *Journal of Geophysical Research: Space Physics*, vol. 121, no. 10, pp. 10,367–10,402, 2016.
- [5] C. E. Duchon, "Lanczos Filtering in One and Two Dimensions," *Journal of Applied Meteorology*, vol. 18, no. 8, pp. 1016–1022, 08 1979.